inorganics

Article

Optimal Choice of the Preparation Procedure and Precursor Composition for a Bulk Ni–Mo–W Catalyst

Ksenia A. Nadeina [1,*], Sergey V. Budukva [1], Yuliya V. Vatutina [1], Polina P. Mukhacheva [1], Evgeniy Yu. Gerasimov [1], Vera P. Pakharukova [1], Igor P. Prosvirin [1], Tatyana V. Larina [1], Oleg V. Klimov [1], Aleksandr S. Noskov [1] and Victor V. Atuchin [2,3,4,5,*]

[1] Surface Science Laboratory, Boreskov Institute of Catalysis, SB RAS, Novosibirsk 630090, Russia
[2] Laboratory of Optical Materials and Structures, Institute of Semiconductor Physics, SB RAS, Novosibirsk 630090, Russia
[3] Research and Development Department, Kemerovo State University, Kemerovo 650000, Russia
[4] Department of Industrial Machinery Design, Novosibirsk State Technical University, Novosibirsk 630073, Russia
[5] R&D Center "Advanced Electronic Technologies", Tomsk State University, Tomsk 634034, Russia
* Correspondence: lakmallow@catalysis.ru (K.A.N.); atuchin@isp.nsc.ru (V.V.A.); Tel.: +7-(383)-3269636 (K.A.N.); +7-(383)-3308889 (V.V.A.)

Abstract: Among the known synthesis procedures and reagents for unsupported Ni–Mo–W catalysts, there is no consensus about optimal preparation conditions of their precursors. In the present work, Ni–Mo–W precursors were prepared via three preparation techniques—hydrothermal synthesis, precipitation method and spray drying—after the synthesis of complex compounds in solution. Ni–Mo–W precursors were studied by the XRD analysis, SEM methods, Raman and UV-vis spectroscopies and XPS measurements and used for the hydrotreatment of straight-run gasoil. Precursors prepared by hydrothermal synthesis contain particles with stacked plate shapes, while other methods provide spherical particles. The formation of different amounts of individual molybdates, tungstates or mixed phases such as $W_{1-x}Mo_xO_3$ possibly doped by Ni was detected. The precipitation technique results in the formation of spheres, with W located at the center and is unavailable for catalysis. The catalytic activity increased when all active metals are available for the feedstock, and a more mixed phase containing Ni, Mo and W is formed. This mixed phase is realized when the synthesis of the Ni–Mo–W precursors is carried out in solution followed by spray drying. The resulting catalyst has 1.2–4 times higher activity than catalysts prepared by other methods.

Keywords: unsupported catalysts; precursors; bulk catalysts; hydrotreating; hydrodesulfurization; hydrodenitrogenation

check for updates

Citation: Nadeina, K.A.; Budukva, S.V.; Vatutina, Y.V.; Mukhacheva, P.P.; Gerasimov, E.Y.; Pakharukova, V.P.; Prosvirin, I.P.; Larina, T.V.; Klimov, O.V.; Noskov, A.S.; et al. Optimal Choice of the Preparation Procedure and Precursor Composition for a Bulk Ni–Mo–W Catalyst. *Inorganics* **2023**, *11*, 89. https://doi.org/10.3390/inorganics11020089

Academic Editors: Franz Edwin López Suárez, Robison Buitrago and Andres F. Suárez

Received: 27 January 2023
Revised: 13 February 2023
Accepted: 16 February 2023
Published: 20 February 2023

1. Introduction

Bulk hydrotreating catalysts have received considerable attention for many years. The characteristic feature of such catalysts is that the active phase content can be 80 to 100 wt.% [1], which is much higher than that of supported catalysts. Since Albemarle company released information about the development of commercial a Ni–Mo–W catalyst in the "Nebula" series that had a much higher catalytic activity in hydrodesulfurization (HDS) and hydrodenitrogenation (HDN) reactions than supported catalysts [2,3], many research contributions have been reported on the synthesis of such bulk catalysts (especially for industrial application) [4–7].

As with all developing catalytic systems, the first question that requires careful consideration is which reagents and methods are preferred for the catalysts preparation. Considering that all components that are added to the system, as well as the conditions of their interactions with each other, can influence the formation of active phases, the investigation of the effect of reagent type is very relevant.

Modern bulk hydrotreating catalysts are mixtures of Ni, Mo and W compounds [6,8–10]. A number of methods are available to prepare such systems. However, these methods are based on the synthesis of an active-phase precursor, the so-called "bulk catalyst precursor". Thus, a method for synthesizing a bulk catalyst by extracting alumina from a $Mo_nW_{12-n}S_2/Al_2O_3$ system was proposed in [11]. However, in this case, the synthesis is complicated by the fact that the supported catalyst is synthesized in the first stage and the support is then removed from the catalyst. The authors of [11] proposed synthesis of the precursor in the reaction mixture by in situ decomposition of oil-soluble metal precursors in a hydrocarbon feedstock. The main difficulty of this method is that the catalyst should be further separated from the liquid oil product.

So-called "wet methods of synthesis" of bulk precursors have become the most widespread. One possible method includes the impregnation of molybdenum sulfide by cobalt nitrate [12] or, on the contrary, impregnation of nickel salt by molybdenum and tungsten compounds [13]. Another more popular method includes simultaneous precipitation of active metal salts. Precipitation in a solution has its several advantages for the preparation of bulk catalysts, such as shorter synthesis time and simpler preparation procedure [14]. Moreover, the reaction conditions can be widely varied. Two such methods were compared in [4]: precipitation under typical conditions under pH-controlled conditions. It was shown that the catalyst obtained under pH-controlled conditions had a larger surface area and a three-dimensional porous structure, providing higher activity in hydrodesulfurization and hydrodenitrogenation reactions. However, the data used in the comparison of the two methods are sufficient to correctly estimate the difference between the obtained precursors. The use of a coprecipitation method is also described in [7,15].

An alternative preparation method for a bulk catalyst precursor is described in [16]. The procedure includes the hydrothermal treatment of a suspension containing previously coprecipitated active metals. The authors state that the use of hydrothermal conditions in the synthesis provides better catalytic properties. Similar preparation methods for a bulk catalyst precursor were used in [6,17,18]. Unfortunately, the procedure has not been compared with other preparation techniques. An attempt to compare the hydrothermal synthesis method and the deposition method was made in [15]. Investigation of two catalyst samples prepared by different methods showed that the sample synthesized under hydrothermal conditions had a high density of exposed active edges, while the sample obtained by precipitation had the most active edges for hydrogenation. All conclusions were made after testing the catalysts in hydrotreating the model feedstock and cannot be reliably applied to a real feedstock.

Obviously, the preparation method is one of the determining factors for the improvement or deterioration of activity. The results obtained in the above-mentioned studies show that the preparation procedure significantly affects the particle shape of the active compound precursor, the formation of transport pores and the distribution of active metals in the catalyst bulk. Nevertheless, it is not possible to compare the results reliably and to reveal the most appropriate preparation procedure for bulk catalyst precursors by combining the data reported in the literature. Moreover, the influence of different metal salts used for synthesis has not been taken into account.

The present work is aimed at the study of the precursors of Ni–Mo–W bulk catalysts synthesized by hydrothermal treatment, the coprecipitation technique and synthesis of the precursor in solution followed by spray drying. Within the hydrothermal method, the optimal preparation conditions and the nature of active metal salts used for the synthesis were determined. The influence of Ni–Mo–W precursor synthesis on the catalyst activity was assessed in the hydrotreatment of real feedstock.

2. Results and Discussion

In the present contribution, the results are reported for bulk catalyst precursors prepared by hydrothermal synthesis ($Ni_1Mo_{0.5}W_{0.5}$–HT–1, $Ni_1Mo_{0.5}W_{0.5}$–HT–2, $Ni_1Mo_{0.5}W_{0.5}$–HT–3, $Ni_1Mo_{0.5}W_{0.5}$–HT–4), the precipitation method ($Ni_1Mo_{0.5}W_{0.5}$–PC) and by spray drying after synthesis in solution ($Ni_1Mo_{0.5}W_{0.5}$–dry). The designation and description of the catalysts are given in Table 1.

Table 1. Description of precursor synthesis.

Precursor	Type of Synthesis	Reagents	Temperature, °C	Reaction Time of Synthesis	Weight Loss upon Ignition, %	Weight of Catalyst Loading in the Reactor per Metal Oxide, g
$Ni_1Mo_{0.5}W_{0.5}$–HT–1	Hydrothermal synthesis	Basic nickel(II) carbonate, AHM, AMT	T of hydrothermal treatment: 170 °C	Hydrothermal treatment: 6 h	7.6	1.85
$Ni_1Mo_{0.5}W_{0.5}$–HT–2		Basic nickel(II) carbonate, MoO_3, H_2WO_4	T of hydrothermal treatment: 150 °C		5.0	1.90
$Ni_1Mo_{0.5}W_{0.5}$–HT–3		Basic nickel(II) carbonate, MoO_3, H_2WO_4	T of hydrothermal treatment: 170 °C		5.5	1.89
$Ni_1Mo_{0.5}W_{0.5}$–HT–4		Basic nickel(II) carbonate, MoO_3, H_2WO_4	T of hydrothermal treatment: 95 °C		7.8	1.84
$Ni_1Mo_{0.5}W_{0.5}$–PC	Direct precipitation	$Ni(NO_3)_3 \cdot 6H_2O$, AHM, AMT	T of solution: 90 °C	Precipitation stage > 12 h	9.9	1.80
$Ni_1Mo_{0.5}W_{0.5}$–dry	Spray drying	$Ni(OH)_2$, CA, AHM, AMT	T of solution at dissolving stage: 70 °C	3 h for dissolution	23.4	1.53

The scanning electron microscopy (SEM) images of the $Ni_1Mo_{0.5}W_{0.5}$–HT–1, $Ni_1Mo_{0.5}W_{0.5}$–PC and $Ni_1Mo_{0.5}W_{0.5}$–dry bulk catalyst precursors are shown in Figures 1–3, respectively. The samples differ considerably in particle morphology. The $Ni_1Mo_{0.5}W_{0.5}$–HT–1 sample is a mixture of particles, which vary in size from very small (about 1 µm) one to about 35 µm. The shape of particles, regardless of their size, resembles stuck plates. Larger particles appear to be more crystallized and "angular" than smaller particles. The $Ni_1Mo_{0.5}W_{0.5}$–PC catalyst precursor contains mostly small spheres with diameters of 1–2.5 µm. Some of the particles seem to be needles, possibly caused by a lack of uniform crystallization. The $Ni_1Mo_{0.5}W_{0.5}$–dry catalyst precursor contains spherical and semispherical particles that are similar in shape to golf balls. The size of the balls is about 2 to 10 µm, but some examples of very large particles (about 25–30 µm) are also seen in the SEM images. Obviously, the preparation technique has a significant influence on the particle morphology [19–22]. Considering only the SEM images, we can assume that samples with a higher surface area of individual particles are more active in the catalysis, but that should be verified by catalytic experiments. The energy-dispersive X-ray (EDX) images (Figures 1–3) of the $Ni_1Mo_{0.5}W_{0.5}$–HT–1, $Ni_1Mo_{0.5}W_{0.5}$–PC and $Ni_1Mo_{0.5}W_{0.5}$–dry bulk catalyst precursors show a uniform distribution of constituent elements over particles. Such uniform distribution is typical of highly active supported catalysts [23,24].

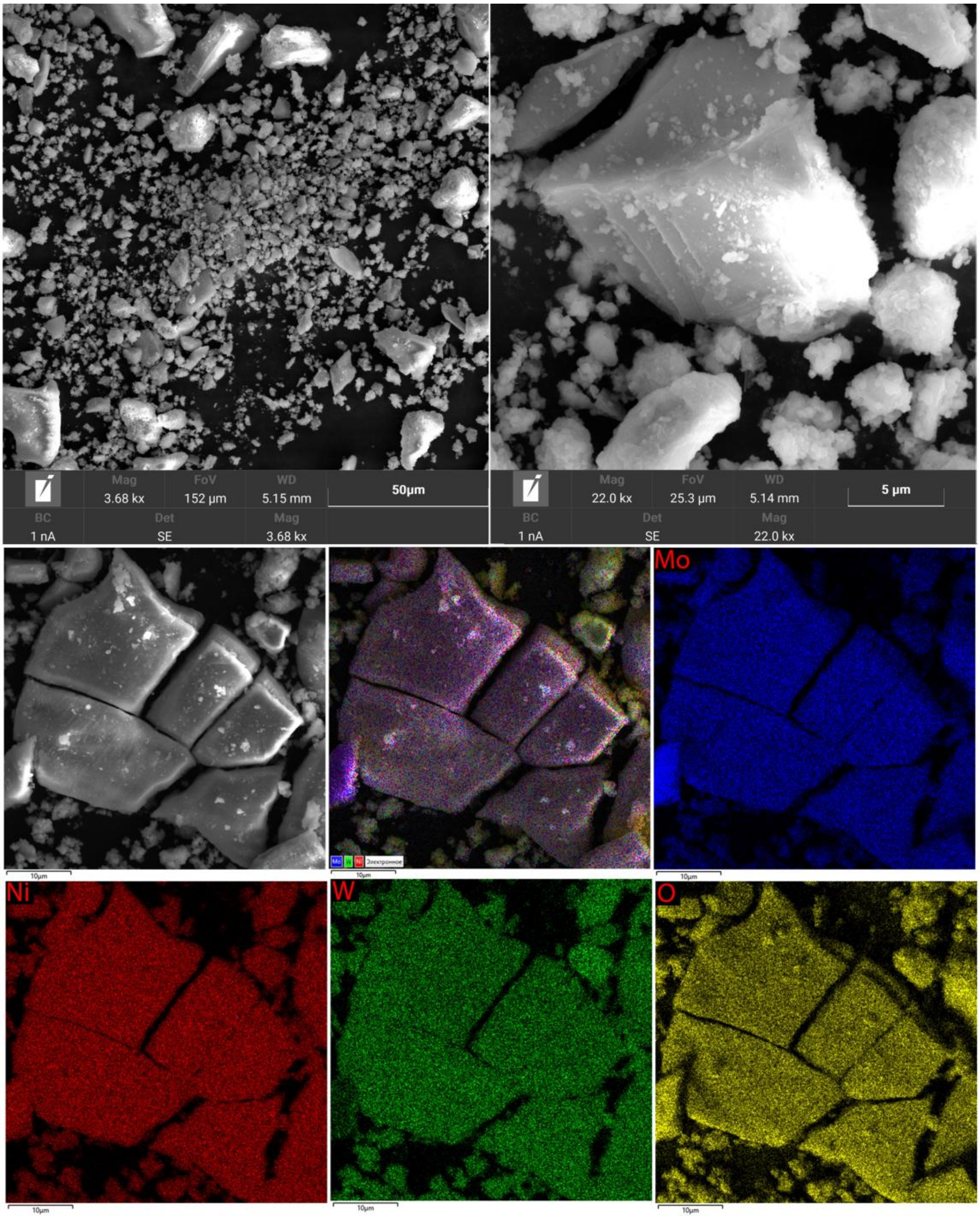

Figure 1. SEM and EDX images of $Ni_1Mo_{0.5}W_{0.5}$–HT–1 catalyst at different resolutions.

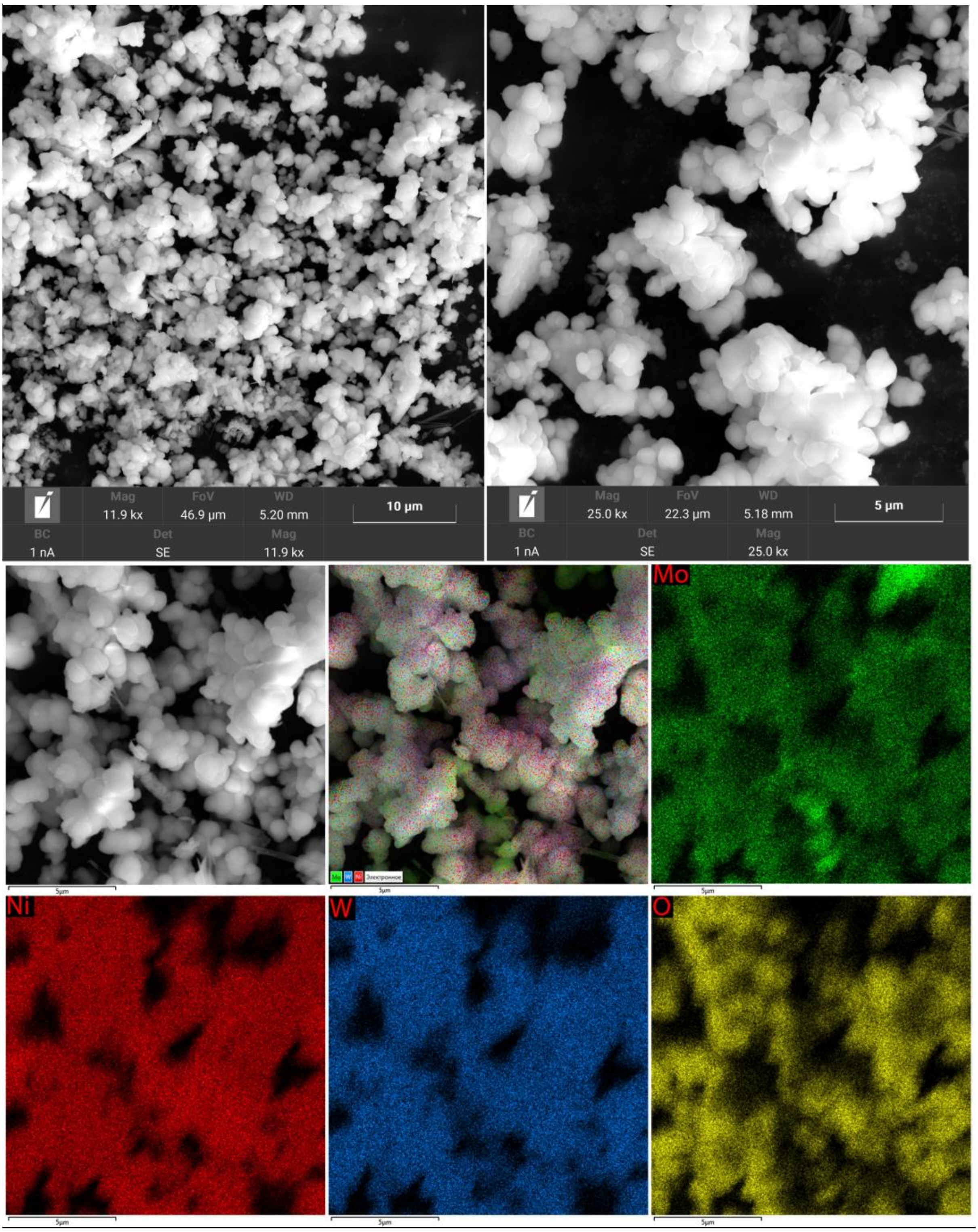

Figure 2. SEM and EDX images of $Ni_1Mo_{0.5}W_{0.5}$–PC catalyst at different resolutions.

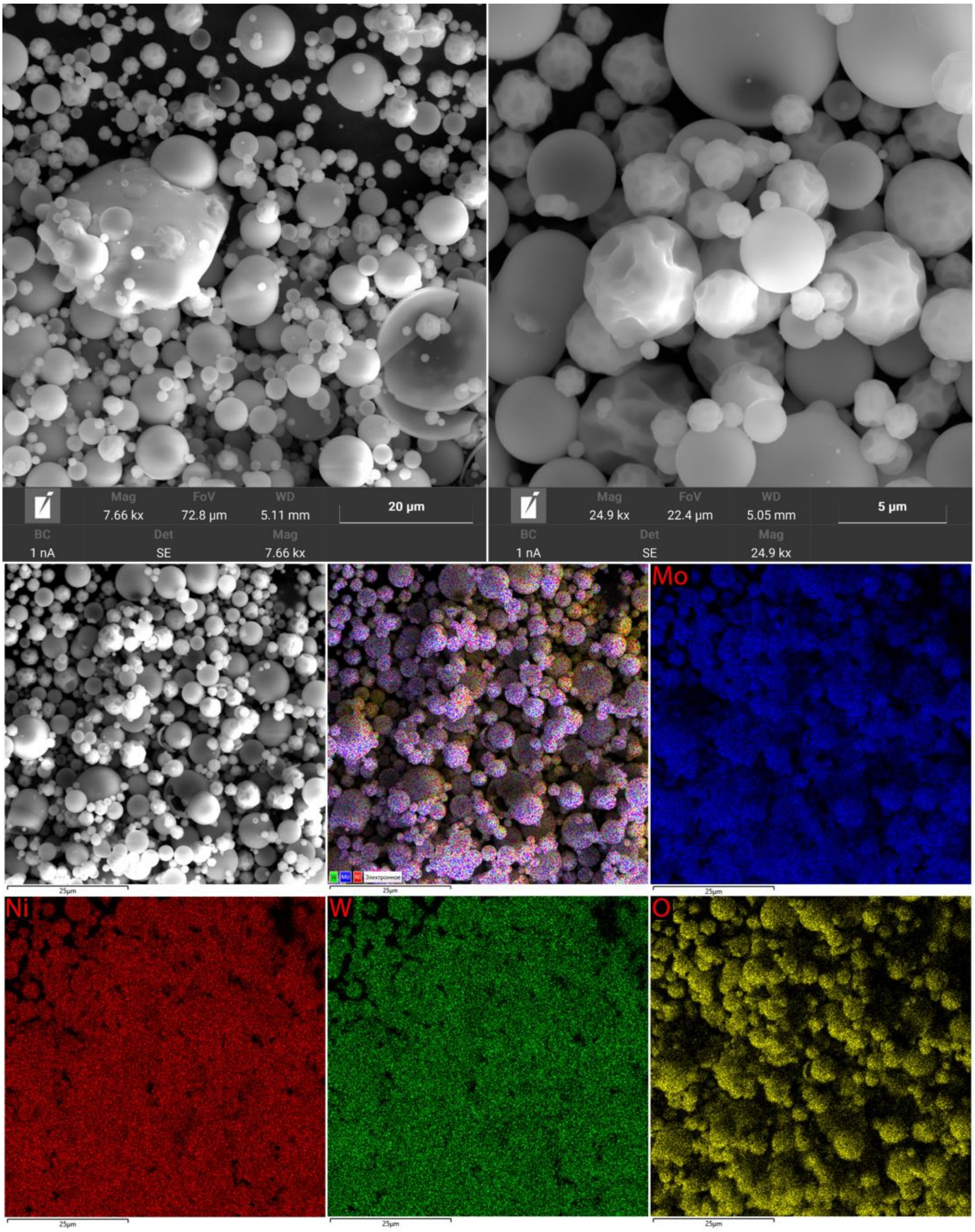

Figure 3. SEM and EDX images of $Ni_1Mo_{0.5}W_{0.5}$–dry (110 °C) catalyst at different resolutions.

X-ray diffraction studies were conducted for precursors dried at 110 °C (or 390 °C for the $Ni_1Mo_{0.5}W_{0.5}$–dry catalyst) and calcined at 500 °C. The first temperature relates to the state of the precursors when they were loaded into the reactor. The calcination temperature was chosen because catalysts undergo higher-temperature regimes during the sulfidation stage and testing. Therefore, we can estimate possible changes in phase composition of the precursors in the reactor and then estimate the phase composition of the active-component precursor.

The X-ray diffraction (XRD) pattern of the $Ni_1Mo_{0.5}W_{0.5}$–HT–1 catalyst is given in Figure 4A. The spectrum contains wide diffuse maxima and narrow peaks. The peaks observed at 16.13, 17.53, 18.38, 23.93 and 28.15° by 2θ can be assigned to the nickel tungstate phase ($NiWO_4$; PDF# 00-015-0755) [6] or to the isostructural phase of nickel molybdate ($NiMoO_4$; PDF# 00-016-0291) [25]. It is also possible that the phase contains both tungsten and molybdenum atoms in the form of $NiW(Mo)O_4$. However, the experimental diffraction pattern is characterized by strong broadening of the most intensive reflection (−111), as well as reflections (010) and (011), which are characteristic of such crystal phases. Similar diffraction patterns were recorded in studies in which the synthesis of nickel tungstate ($NiWO_4$) by the hydrothermal procedure [26,27] and the precipitation technique [28] was followed by drying at a low temperature. The observed features in the X-ray diffraction patterns can be explained by a poor $NiWO_4$ phase crystallization degree. The well-crystallized phase of nickel tungstate ($NiWO_4$) was formed after calcination at a higher temperature of 600 °C [27,28]. These data strongly support the XRD data.

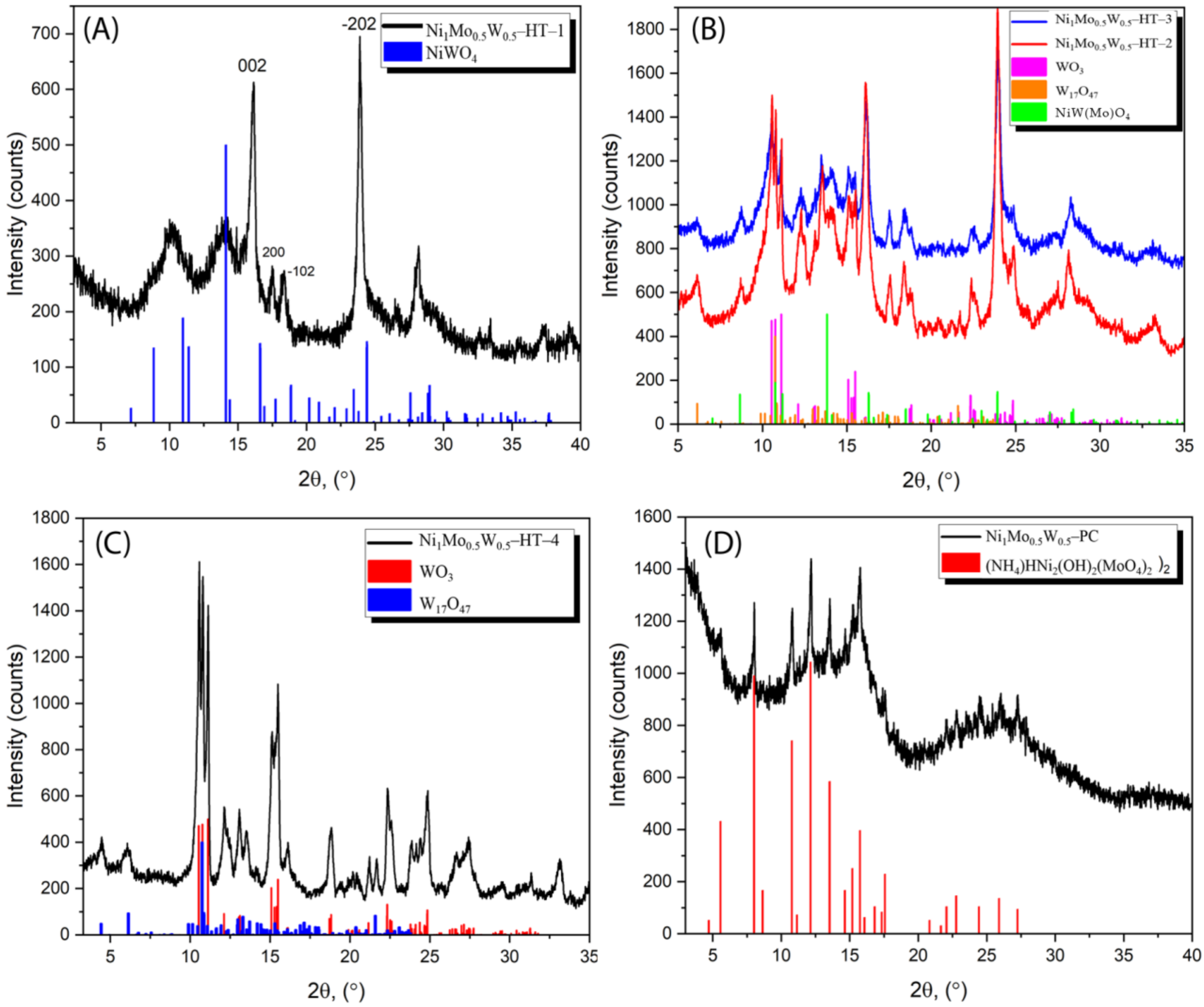

Figure 4. X-ray diffraction patterns: (**A**) $Ni_1Mo_{0.5}W_{0.5}$–HT–1, (**B**) $Ni_1Mo_{0.5}W_{0.5}$–HT–2 and $Ni_1Mo_{0.5}W_{0.5}$–HT–3, (**C**) $Ni_1Mo_{0.5}W_{0.5}$–HT–4 and (**D**) $Ni_1Mo_{0.5}W_{0.5}$–PC catalysts.

Since the peaks at (−111), (010), (01−1), (110), (−112) and (−211) are anomalously broadened with a non-zero k index value, it can be suggested that there is poor crystallinity in the crystallographic direction [010], which may caused by the preservation of strong hydration (presence of water molecules or hydroxyl groups in the structure). The presence of residual hydroxyl groups or water molecules can be also indicated by a change in the crystal lattice. Indeed, in the experimental XRD pattern, a shift of the (002), (200), (−102) and (−202) peaks to lower angles is detected, which indicates an increase in the crystal cell parameters.

The diffraction patterns of the $Ni_1Mo_{0.5}W_{0.5}$–HT–2 and $Ni_1Mo_{0.5}W_{0.5}$–HT–3 samples are presented in Figure 4B. According to the XRD data, the samples contain a tungsten oxide phase of WO_3 (PDF# 00-020-1323) [29], in addition to a $NiW(Mo)O_4$ phase. It is possible that this oxide is also related to mixed oxides such as $W_{1-x}Mo_xO_3$ since there is an isostructural crystalline phase of molybdenum oxide (MoO_3; PDF# 00-65-7675). Moreover, the samples contain a phase of tungsten oxide with the composition $W_{17}O_{47}$ (PDF# 00-044-0396) [30]. Measuring coherent scattering region (CSR) values is difficult because of a strong overlapping of the peaks.

The diffraction patterns of the $Ni_1Mo_{0.5}W_{0.5}$–HT–4 catalyst are shown in Figure 4C. The crystalline $NiW(Mo)O_4$ phase is absent in the sample because its characteristic diffraction peaks were not detected. The sample contains impure WO_3 (or $W_{1-x}Mo_xO_3$) and $W_{17}O_{47}$ oxide phases.

The X-ray diffraction pattern of the $Ni_1Mo_{0.5}W_{0.5}$–PC catalyst is shown in Figure 4D. The narrow maxima in the spectrum are characteristic of a $(NH_4)HNi_2(OH)_2(MoO_4)_2$ crystal phase (PDF#00-050-1414, $R\bar{3}m$, a = b = 6.015 Å, c = 21.881 Å) [31]. This crystal phase is related to the laminate Φ_y phase with a hexagonal structure [32]. The average CSR size is D_{XRD} = 30 nm. The overall view of the X-ray pattern (presence of diffusion scattering) indicates the presence of amorphous X-ray compounds, possibly containing W.

The XRD patterns of the $Ni_1Mo_{0.5}W_{0.5}$–dry catalyst calcined at 390 and 500 °C are given in Figure 5. The $Ni_1Mo_{0.5}W_{0.5}$–dry catalyst dried at 390 °C, as well as that dried at 110 °C, (not shown in Figure 6) is X-ray-amorphous. Therefore, we calcined the sample at 500 °C to deduce which phases can be crystallized at higher temperatures. The following crystal phases were detected in the X-ray diffraction patterns of the $Ni_1Mo_{0.5}W_{0.5}$–dry catalyst calcined at 500 °C: (1) α–$NiMoO_4$ (PDF#00-033-0948, a = 9.509 Å, b = 8.759 Å, c = 7.667 Å) with D_{XRD} = 10 nm [6]; (2) WO_3 (PDF#00-033-1387, a = b = 7.298 Å, c = 3.899 Å) with D_{XRD}~8 nm [33]; (3) $NiWO_4$ (PDF#00-015-0755, a = 4.912 Å, b = 4.60 Å, c = 5.665 Å) with D_{XRD} = 19 nm [34]; (4) NiO (PDF#00-047-1049, a = b = c = 4.177 Å) with D~10 nm [35]. It should be noted that α–$NiMoO_4$ prevails in the catalyst.

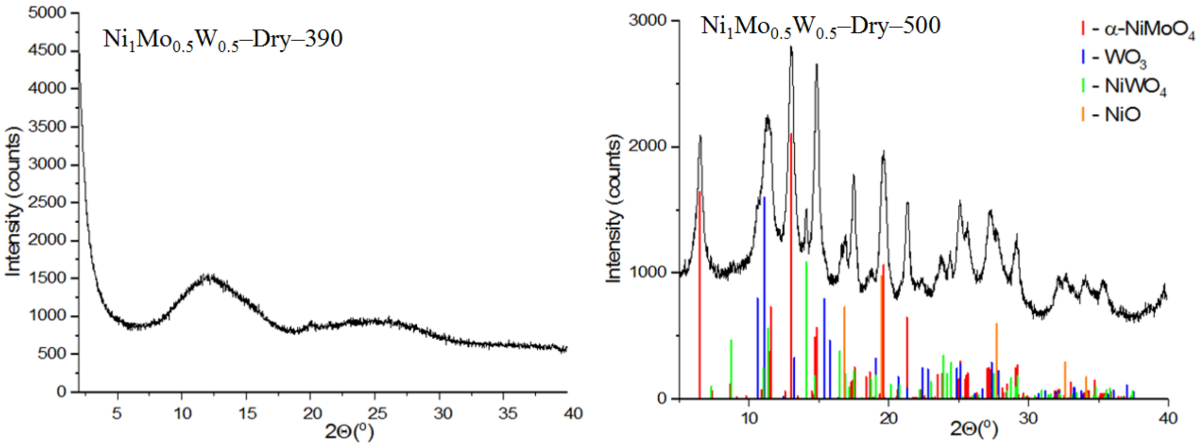

Figure 5. X-ray diffraction pattern of the $Ni_1Mo_{0.5}W_{0.5}$–dry catalyst calcined at 390 and 500 °C.

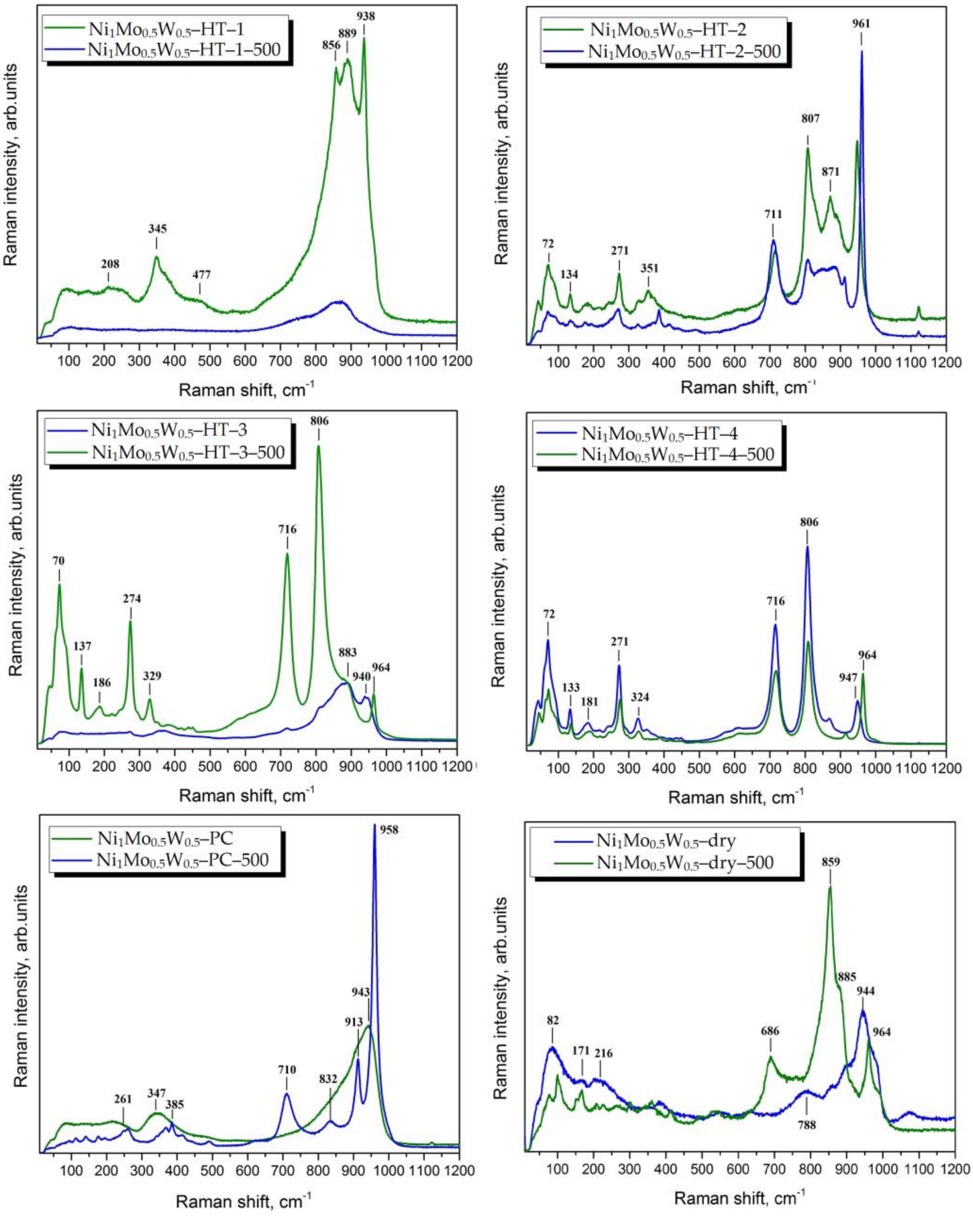

Figure 6. Raman spectra of catalyst precursors dried at different temperatures.

Catalysts dried at different temperatures were evaluated by Raman spectroscopy. The $Ni_1Mo_{0.5}W_{0.5}$–HT–1, $Ni_1Mo_{0.5}W_{0.5}$–HT–2, $Ni_1Mo_{0.5}W_{0.5}$–HT–3, $Ni_1Mo_{0.5}W_{0.5}$–HT–4, $Ni_1Mo_{0.5}W_{0.5}$–PC and $Ni_1Mo_{0.5}W_{0.5}$–dry catalysts were studied at preparation temperatures of 110 °C and 500 °C. The second temperature was chosen to understand the changes that occurred in the reactor during the sulfidation stage.

Figure 6 clearly shows that the preparation technique and reagents have a significant effect on the Raman spectra and, therefore, on the structure of the precursors. The spectrum of the $Ni_1Mo_{0.5}W_{0.5}$–HT–1 sample dried at 110 °C contains a wide band at 700–1000 cm^{-1} with strong maxima at 856, 889 and 938 cm^{-1}. The band at 938 cm^{-1} corresponds to symmetric and antisymmetric stretching of υ(Mo=O) in molybdenum ions in the tetrahedron coordination of oxygen atoms, which is typical of many molybdates [36,37]. The bands at 889 and 856 cm^{-1} are attributed to the asymmetric bending modes in O–Mo–O bonds. Similar vibrations were observed for the hydrated $NiMoO_4$ phase [26,36]. The presence of α– and β–$NiMoO_4$ phases should not be excluded. The presence of the intensive band at 952–960 cm^{-1} and less intensive bands at 938 and 900–912 cm^{-1} are typical of these phases [36].

The band at 345 cm^{-1} with a small shoulder can be assigned to the asymmetric and symmetric bending modes of O–Mo–O, but it can overlap the band from the symmetric vibration of NiO_6 octahedra [26]. The signal at 208 cm^{-1} corresponds to the bending W–O–W mode, while the bands in the range of 880–1000 cm^{-1} can be assigned to the symmetric W=O stretching of the WO_6 units [38,39]. In general, the spectrum of the $Ni_1Mo_{0.5}W_{0.5}$–HT–1 sample dried at 110 °C seems to be the superposition of the spectra of α– and β–$NiMoO_4$ and $NiWO_4$. When the temperature is increased to 500 °C, most vibrations disappear, and only vibrations at 700–950 cm^{-1} are observed. It is noted that in this case, the vibrations of the Ni–O–Mo bond at 760 cm^{-1} are more intense. It is possible that the sample becomes more amorphous.

When we change reagents for the synthesis ($Ni_1Mo_{0.5}W_{0.5}$–HT–3 sample), the Raman spectra are also significantly altered (Figure 6). It was clearly shown in [36] that such variations in Raman spectra can be observed when the ratio of α– and β–$NiMoO_4$ modifications changes. The bands characteristic for Mo–O, O–Mo–O and Ni–Mo–O vibrations in the α–$NiMoO_4$ phase (883, 716 and 274 cm^{-1}) become more pronounced in the spectra of the $Ni_1Mo_{0.5}W_{0.5}$–HT–3 sample. In addition, the presence of bands in the range of 880–970 cm^{-1} and clearly observable bands in the range of 180–280 cm^{-1} can be associated with $NiWO_4$ [40]. It should be noted that the bands at 100–300 cm^{-1}, as well as some peaks at 800–1000 cm^{-1}, can be also related to the octahedral MoO_6 modes in crystalline MoO_3 [41,42] and to the monoclinic crystalline WO_3 phase [43]. According to the XRD data, this sample may also contain a mixed $W_{1-x}Mo_xO_3$ phase and $W_{17}O_{47}$ oxide. Therefore, such changes in the spectrum can be explained by the formation of additional phases. The increase in the thermal treatment temperature results in the disappearance of most of the peaks. Only the bands at 800–1000 cm^{-1} remain in the spectra related to the vibrations of $NiMoO_4$ and $NiWO_4$ compounds. Due to the fact that the observed bands are characteristic of β–$NiMoO_4$ modification and $NiWO_4$ and not of α–$NiMoO_4$, it is possible to conclude that α–$NiMoO_4$ disappears from the precursor at a higher temperature or its concentration is considerably reduced.

The decrease in the temperature of hydrothermal treatment to 150 °C (the $Ni_1Mo_{0.5}W_{0.5}$–HT–2 sample) resulted in an increase in the peak intensity at 940–960 cm^{-1} from the β–$NiMoO_4$ modification, while other peaks were persistent in their intensity and ratio (Figure 6). We can suggest that a lower temperature is preferable for the formation of β–$NiMoO_4$. The XRD data of the $Ni_1Mo_{0.5}W_{0.5}$–HT–2 sample also show the presence of some mixed phases such as in the $Ni_1Mo_{0.5}W_{0.5}$–HT–3 sample. However, it is not possible to distinguish the ratio of these phases. It is also noted that the changes in the calcination temperature slightly affect the peak intensity. Therefore, the sample composition is sufficiently stable at the exposure temperature. A further decrease in the hydrothermal treatment temperature to 95 °C (the $Ni_1Mo_{0.5}W_{0.5}$–HT–4 sample) results in a reduction in the peak intensity of all spectra, although their location and ratio seem to be the same. The lower peak intensity may be caused by the weaker crystallinity of the obtained phases. Combined consideration of Raman and XRD data allows us to conclude that the sample contains WO_3 and $W_{17}O_{47}$ crystal oxide phases and possibly a mixed $W_{1-x}Mo_xO_3$ phase.

The $Ni_1Mo_{0.5}W_{0.5}$–PC sample dried at 110 °C is significantly different from the HT series (Figure 6). The sharp band in the range of 700–1000 cm^{-1} can be related to Mo–O vibrations. The Raman spectrum, in conjunction with the XRD data, allows us to suggest that the observed bands correspond to a complex $(NH_4)HNi_2(OH)_2(MoO_4)_2$ compound. The bands from the tungsten–containing phase cannot be individually revealed. When the temperature is relatively high (500 °C), the peaks from the $NiMoO_4$ and $NiWO_4$ phases are observed.

The spectrum of the $Ni_1Mo_{0.5}W_{0.5}$–dry catalyst dried at 110 °C contains bands of $NiMoO_4$ and $NiWO_4$ phases (Figure 6). It is noted that the observed peaks are more typical of the β–$NiMoO_4$ phase than of the α–$NiMoO_4$ phase. On the contrary, the calcination of the catalyst results in the enhancement of vibrations from the α–$NiMoO_4$ phase. The spectra of the calcined catalyst are similar to those described in [44] for regenerated supported catalysts.

The results of ultraviolet-visible diffuse reflectance spectroscopy (UV-vis DRS) measurements carried out for the catalyst precursors are shown in Figure 7. Two adsorption regions can be pointed out: a visible part of the spectrum in the range of 900–380 nm and a UV region in the range of 380–190 nm. The absorption bands in the UV region between 200 and 400 nm can be assigned to the ligand-to-metal charge transfer (LMCT) (O^{2-}—W^{6+}) and (O^{2-}—Mo^{6+}) in Mo^{6+} and W^{6+} cations in the tetrahedral and octahedral coordinations, which are difficult to unambiguously separate from each other. In addition, these adsorption bands are related to (O^{2-}—Ni^{2+}) transitions in the octahedral coordination ($Ni^{2+}{}_{Oh}$). In particular, the region between 200 and 280 nm corresponds to the tetrahedral coordination of W and Mo in the $[MoO_4]/[WO_4]$ domains, as well as to LMCT bands in $Ni^{2+}{}_{Oh}$ cations. The bands from $[MoO_6]/[WO_6]$ domains are located at 280–370 nm [45–47]. The influence of the preparation method and reagents on the UV-vis diffuse reflection spectra are shown in Figure 7. The UV-vis DR spectra of the $Ni_1Mo_{0.5}W_{0.5}$–dry and $Ni_1Mo_{0.5}W_{0.5}$–PC catalysts contain two narrow LMCT bands at 220 and 280 nm characteristic of isolated and distorted tetrahedral domains $[MoO_4]/[WO_4]$ and octahedral domains $[NiO_6]$, respectively. These structures are features of laminated nickel molybdates or tungstates [31], as well as of carboxylic nickel complex compounds [48]. The $Ni_1Mo_{0.5}W_{0.5}$–HT–1 sample is characterized by a wide LMCT band with a maximum at 330 nm and a small shoulder at 235 nm, which can be attributed to octahedral $[MoO_6]/[WO_6]$ clusters. These clusters are related to the prolonged chains of MoO_3/WO_3 oxides [49,50].

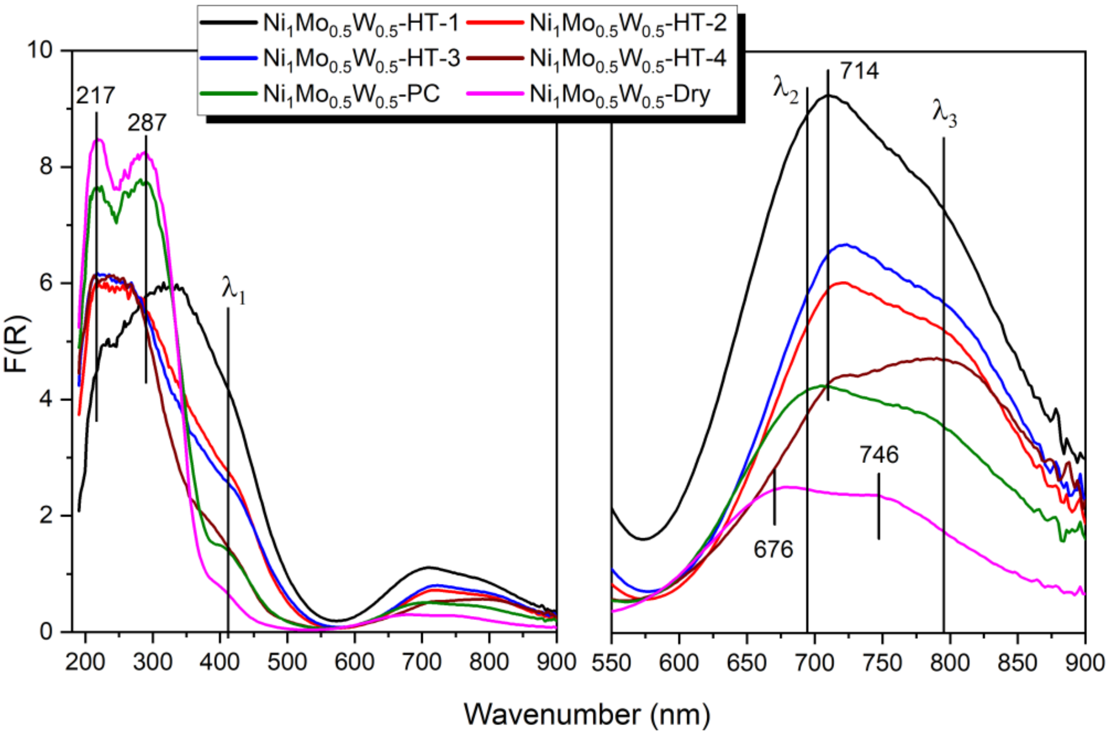

Figure 7. UV-vis DR spectra of catalyst precursors dried at 110 °C.

The series of the samples synthesized by the hydrothermal method show LMCT bands with a similar value of the adsorption maximum in the range of 220–285 nm. It also corresponds to the isolated octahedral [NiO_6] clusters characteristic of nickel molybdate and/or tungstate. The absorption edge of polyhedral Mo/W shifts to longer wavelengths (red shift) in the following order of samples: $Ni_1Mo_{0.5}W_{0.5}$–HT–4 > $Ni_1Mo_{0.5}W_{0.5}$–HT–3 > $Ni_1Mo_{0.5}W_{0.5}$–HT–2 > $Ni_1Mo_{0.5}W_{0.5}$–PC = $Ni_1Mo_{0.5}W_{0.5}$–dry > $Ni_1Mo_{0.5}W_{0.5}$–HT–1. The red shift is possibly caused by the increase in the average size of Mo/W domains in the precursors.

In the visible part of the UV-vis spectrum in the range of 400–900 nm, there are adsorption bands related to d–d transitions in Ni^{2+} cations in the octahedral oxygen coordination ($Ni^{2+}{}_{Oh}$). The cations are stabilized in different compounds (seen in XRD), which differ in their composition because of the preparation conditions. The first permitted transition ($^3T_g(F)$—$^3T_{1g}(F)$; λ_3—794–746 nm), the second forbidden transition ($^3T_g(F)$—$^1T_{1g}(F)$; λ_2—714–676 nm) and the third weakly permitted transition ($^3T_g(F)$—$^3T_{1g}(P)$; λ_1—407 nm) were detected. The $Ni^{2+}{}_{Oh}$ cations in the series of precursors synthesized under hydrothermal conditions are likely stabilized in the $NiMoO_4$ and $NiWO_4$ phases, in agreement with the XRD data. The decrease in the adsorption band intensity at 714 nm may indicate an increase in the degree of the order of $Ni^{2+}{}_{Oh}$ cations in the first coordination sphere or a decrease in the distortion degree of the octahedral surrounding of $Ni^{2+}{}_{Oh}$ cations. Wider and more intensive bands (in comparison with the adsorption band at 719 nm) appear at 794 nm in the spectra of the $Ni_1Mo_{0.5}W_{0.5}$–HT–4 sample, which indicates another type of stabilization of $Ni^{2+}{}_{Oh}$ cations. The $Ni^{2+}{}_{Oh}$ cations in this catalyst are most likely stabilized in the form of an X-ray-amorphous NiO phase, which should be more pronounced in the UV-vis spectra of catalysts calcined at higher temperatures.

In addition, a red shift is observed in the series $Ni_1Mo_{0.5}W_{0.5}$–dry > $Ni_1Mo_{0.5}W_{0.5}$–PC > $Ni_1Mo_{0.5}W_{0.5}$–HT–2 = $Ni_1Mo_{0.5}W_{0.5}$–HT–4 = $Ni_1Mo_{0.5}W_{0.5}$–HT–3 > $Ni_1Mo_{0.5}W_{0.5}$–HT–1. According to the spectrochemical series, this bathochromic shift is associated with the replacement of –COO– (–COOH) (in the $Ni_1Mo_{0.5}W_{0.5}$–dry) or NH_3 (in the $Ni_1Mo_{0.5}W_{0.5}$–PC) ligands in the nickel ion with weaker ligands, such as H_2O or Mo(W)O– in the series of the samples synthesized under hydrothermal conditions. Therefore, the decrease in the absorption band intensity at 330–500 nm for the $Ni_1Mo_{0.5}W_{0.5}$–HT–x series indicates an increase in the crystallinity degree from $Ni_1Mo_{0.5}W_{0.5}$–HT–1 to the $Ni_1Mo_{0.5}W_{0.5}$–HT–4, in agreement with the XRD data. In the spectra of the $Ni_1Mo_{0.5}W_{0.5}$–dry and $Ni_1Mo_{0.5}W_{0.5}$–PC catalysts, there is a sharp adsorption edge at 370 nm, which evidences the prevalence of Mo^{6+}/W^{6+} cations in the tetrahedral coordination (wide adsorption bands at 217–287 nm) in the new structure formed during synthesis.

Thermogravimetry (TG) and derivative thermogravimetry (DTG) curves of the precursors of bulk catalysts in their dried form are shown in Figure 8. It is clearly seen that the preparation procedure and reagents have a considerable effect on the TGA curves. The curves for the $Ni_1Mo_{0.5}W_{0.5}$–HT–x series can be divided into three ranges: 50–140, 150–350 and 400–600 °C. The weight loss at 50–140 °C is caused by the loss of weakly adsorbed water. A considerable difference in the DTG curve in the range of 140–450 °C is observed for the $Ni_1Mo_{0.5}W_{0.5}$–HT–1 catalyst. There are 10 low-intensity exo- and endo-effects, which are difficult to identify. These exo- and endo-effects are most likely caused by the elimination of water from various Ni, Mo and W compounds. The other samples in the series are characterized by one endo-effect at 300 °C due to the elimination of structural water.

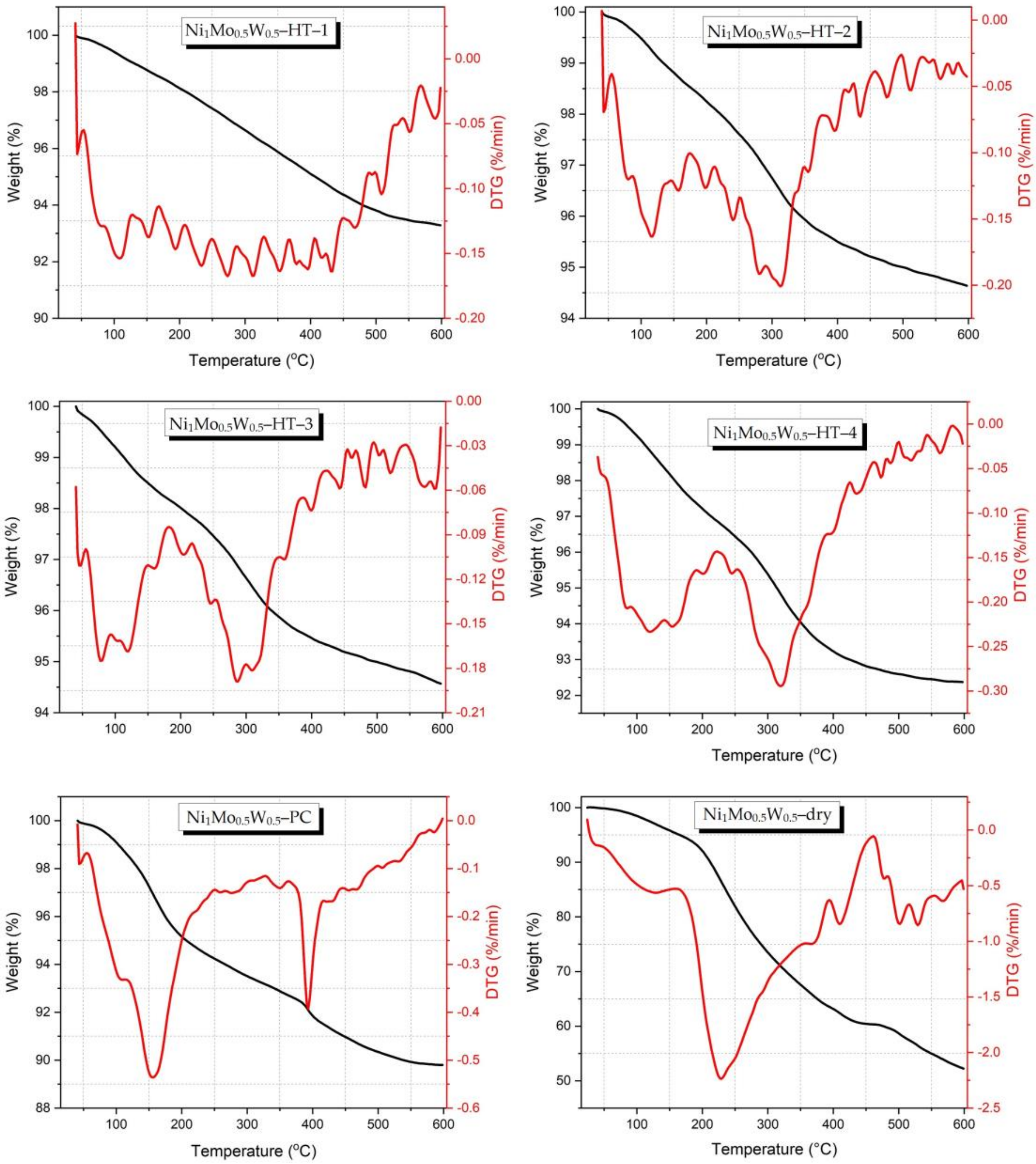

Figure 8. TG/DTG curves of catalyst precursors dried at 110 °C.

The $Ni_1Mo_{0.5}W_{0.5}$–PC catalyst is characterized by two pronounced endo-effects on the DTG curve. The first one at 100 °C is related to the elimination of adsorbed water and ammonia. The second one at 400 °C is assigned to the elimination of structural water and decomposition of $(NH_4)HNi_2(OH)_2(MoO_4)_2$ or some amorphous W–containing structures.

The DTG curve of the $Ni_1Mo_{0.5}W_{0.5}$–dry sample is characteristic of the decomposition of citrate ligands [51–53]. The weight loss at 50–150 °C is related to the removal of adsorbed water and ammonia. Considerable weight loss (25% of the total weight) is observed at 180–350 °C due to the decomposition of citrate ligands to complex acetonedicarboxylate compounds or oxycarbonate compounds [51,54]. The complete decomposition of citrate complexes occurs at ~300 °C. Weight loss at temperatures over 400–600 °C is accompanied by a strong exo-effect, which is related to the oxidation of residual fragments of organic molecules and amorphous carbon and to the formation of nickel, molybdenum and tungsten oxides, as well as their phase transitions [55–57].

The residual sulfur and nitrogen contents in the product are given in Figure 9A,B. However, the direct estimation of the catalytic activity from the residual sulfur content is not completely correct because the catalysts exhibit varying weight loss upon ignition (Table 1), resulting in varying contents of active metals in catalyst loadings. Therefore, the hydrodesulfurization rate constant (k_{HDS}) was also calculated using Equations (1) and (2) (see Section 3.3). The obtained results are shown in Figure 9C.

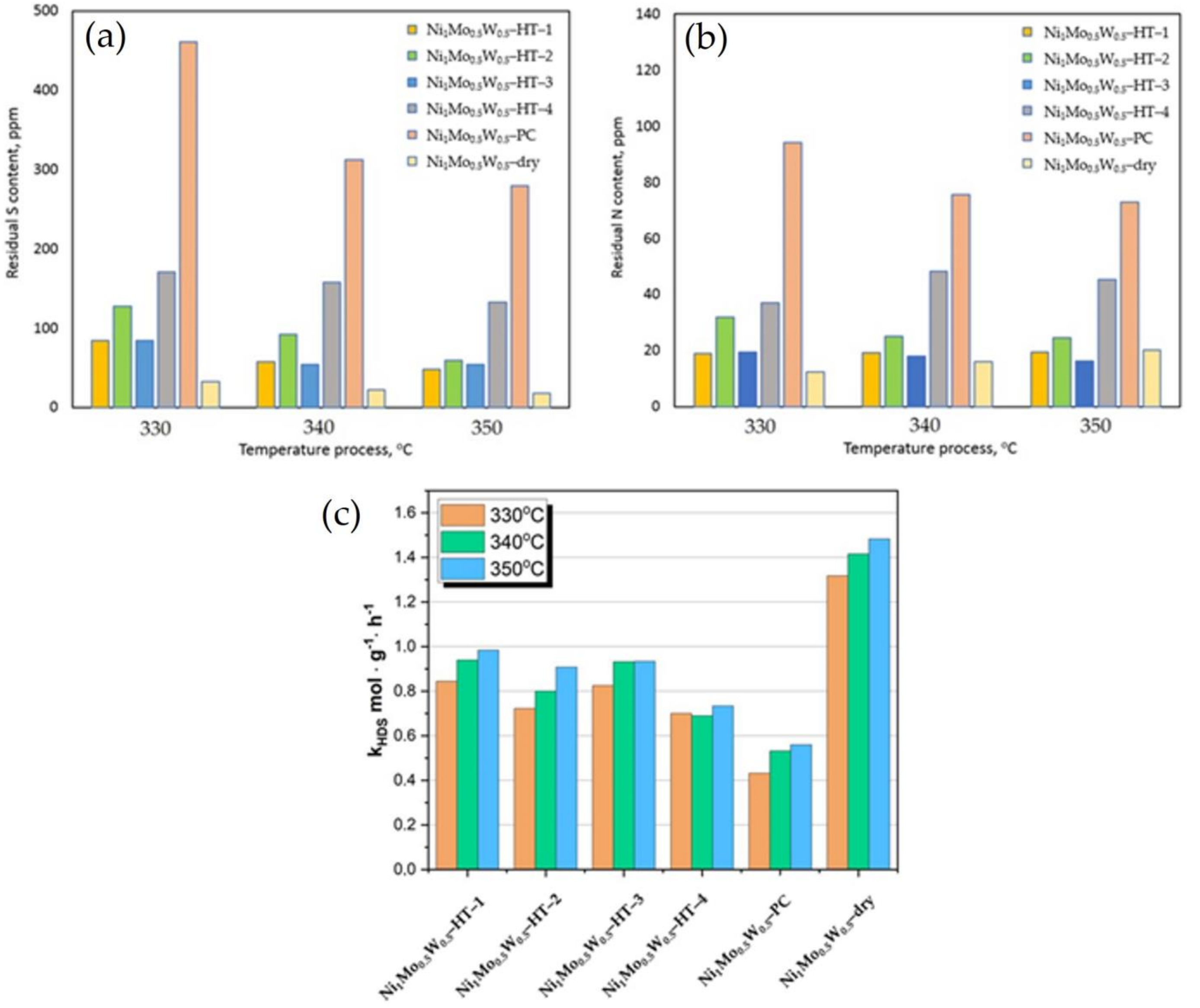

Figure 9. Residual sulfur (**A**) and nitrogen (**B**) content in the liquid product after the hydrotreatment and HDS rate constants for sulfide catalysts (**C**).

In the studied catalyst series, the $Ni_1Mo_{0.5}W_{0.5}$–PC catalyst was the least active in hydrodesulfurization reactions (Figure 9). The HDS activity increased in the following order: $Ni_1Mo_{0.5}W_{0.5}$–PC < $Ni_1Mo_{0.5}W_{0.5}$–HT–4 < $Ni_1Mo_{0.5}W_{0.5}$–HT–2 < $Ni_1Mo_{0.5}W_{0.5}$–HT–3 < $Ni_1Mo_{0.5}W_{0.5}$–HT–1 < $Ni_1Mo_{0.5}W_{0.5}$–dry. The observed dependences for rate constants correlate with the residual sulfur content in hydrotreated products. It should be noted that the activity trends obtained for the HDS reaction are exactly the same for the HDN reactions. The lowest residual sulfur and nitrogen contents in the hydrotreated product were obtained for the $Ni_1Mo_{0.5}W_{0.5}$–dry catalyst.

To distinguish the difference between more and less active catalysts, X-ray photoelectron spectroscopy (XPS) studies were carried out for the $Ni_1Mo_{0.5}W_{0.5}$–HT–3, $Ni_1Mo_{0.5}W_{0.5}$–PC and $Ni_1Mo_{0.5}W_{0.5}$–dry samples. After the catalytic test, the catalysts were washed by hexane before XPS measurements. The obtained Mo3d+S2s, Ni2p and W4f spectra were decomposed to various metal states (Figure 10). The binding energies for the most intensive photoelectron signals of $Mo3d_{5/2}$, $Ni2p_{3/2}$ and $W4f_{7/2}$ states, as well as the calculated relative content of metals in different states, are given in Table 2.

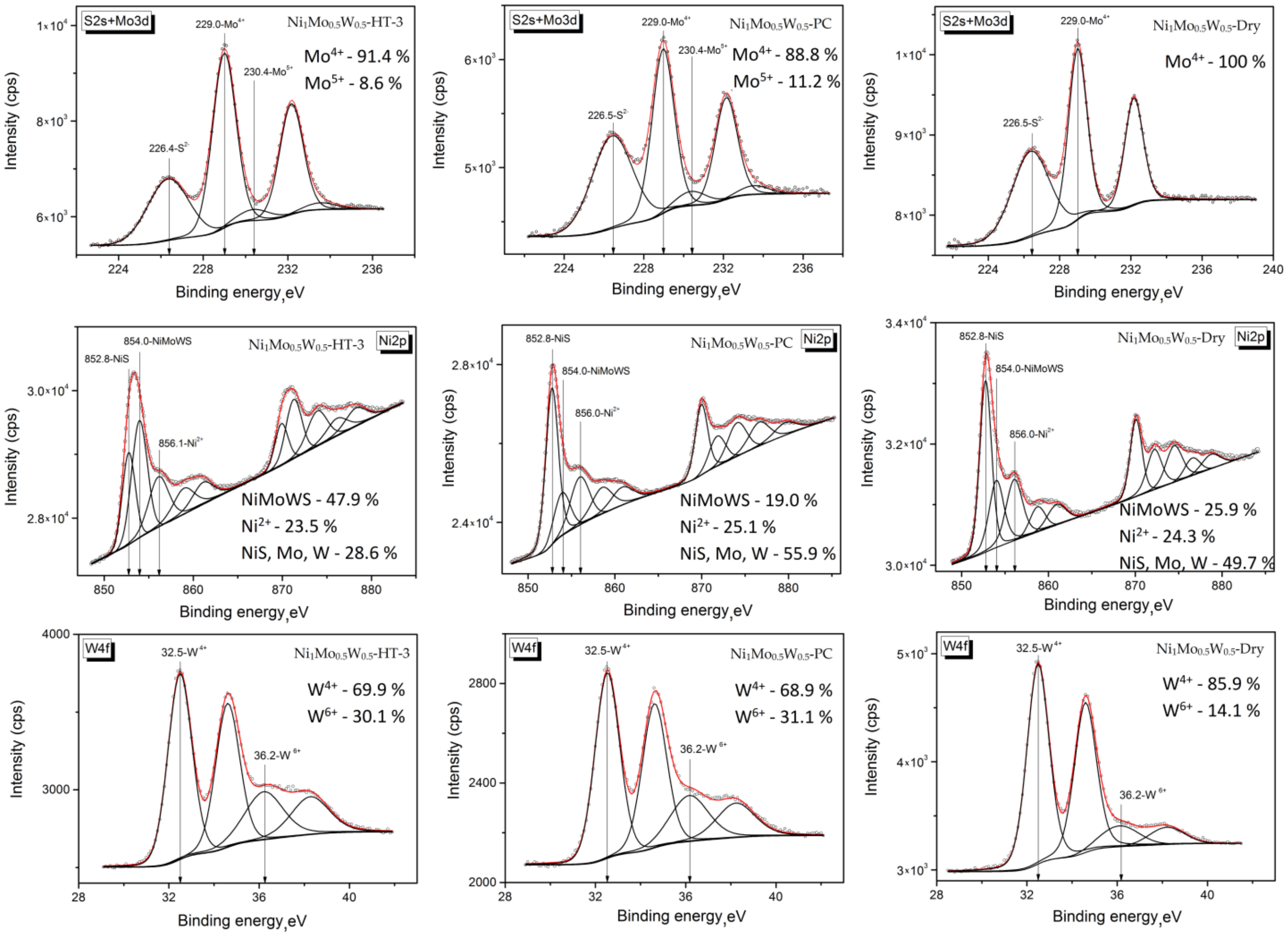

Figure 10. XPS spectra of the $Ni_1Mo_{0.5}W_{0.5}$–HT–3, $Ni_1Mo_{0.5}W_{0.5}$–PC and $Ni_1Mo_{0.5}W_{0.5}$–dry catalyst precursors recorded after catalytic tests.

Table 2. XPS data for $Ni_1Mo_{0.5}W_{0.5}$–HT–3, $Ni_1Mo_{0.5}W_{0.5}$–PC and $Ni_1Mo_{0.5}W_{0.5}$–dry.

Catalyst	$Ni_1Mo_{0.5}W_{0.5}$–HT–3	$Ni_1Mo_{0.5}W_{0.5}$–PC	$Ni_1Mo_{0.5}W_{0.5}$–Dry
BE of $Mo^{4+}{}_{3d5/2}$, eV	229.0 ± 0.1		
BE of $Mo^{5+}{}_{3d5/2}$, eV	230.4 ± 0.1		
BE of $Mo^{6+}{}_{3d5/2}$, eV	232.7 ± 0.1		
Mo^{4+}, %	91.4	88.8	100.0
Mo^{5+}, %	8.6	11.2	0
Mo^{6+}, %	0	0	0

Table 2. *Cont.*

Catalyst	$Ni_1Mo_{0.5}W_{0.5}$–HT–3	$Ni_1Mo_{0.5}W_{0.5}$–PC	$Ni_1Mo_{0.5}W_{0.5}$–Dry
BE of NiMoWS, eV		854.0 ± 0.1	
BE of Ni^{2+}, eV		856.0 ± 0.1	
BE of NiS, eV		852.8 ± 0.1	
NiMoWS, %	47.9	19.0	25.9
Ni^{2+}, %	23.5	25.1	24.3
NiS, Mo, W, %	28.6	55.9	49.7
BE of $W^{4+}{}_{4f7/2}$, eV		32.5 ± 0.1	
BE of $W^{6+}{}_{4f7/2}$, eV		36.2 ± 0.1	
W^{4+}, %	69.9	68.9	85.9
W^{6+}, %	30.1	31.1	14.1
Mo/S	0.28	0.18	0.15
Ni/S	0.24	0.52	0.27
W/Mo	2.34	0.61	1.04
W/Ni	2.0	0.2	1.9

According to the decomposition of the Mo3d+S2s spectra, the binding energies of the Mo3$d_{5/2}$ (229.0 ± 0.1 eV) and Mo3$d_{3/2}$ (232.1 ± 0.1 eV) [58] components are characteristic of molybdenum in the form of an MoS_2 phase [59,60]. The band with a binding energy (BE) of 226.4 ± 0.1 eV is related to the contribution of S2s for S^{2-} in MoS_2 and that of $S_2{}^{2-}$ in MoO_xS_y [59,61]. The spectra were decomposed into three molybdenum states: Mo^{4+}, Mo^{5+} and Mo^{6+}. However, only Mo^{4+} and Mo^{5+} were detected in catalysts, and the Mo^{4+} state was dominant in catalysts. Its content varies in the range of 88.8–100%. The highest value was obtained for the $Ni_1Mo_{0.5}W_{0.5}$–dry sample (100%). The content of the Mo^{5+} state is about 8.6–11.2%. This state of Mo was not observed in the $Ni_1Mo_{0.5}W_{0.5}$–dry sample.

Analysis of the W4f spectra shows that the BE values 32.5 ± 0.1 eV (W4$f_{7/2}$) and 34.6 ± 0.1 eV (W4$f_{5/2}$) [62,63] correspond to the W^{4+} state in the sulfide composition, which confirms the conversion of WO_3 to WS_2 during the sulfidation stage [64]. The contributions of W4$f_{7/2}$ (36.2 ± 0.1 eV) and W4$f_{5/2}$ (38.2 ± 0.1 eV) states corresponding to W^{6+} in the oxide composition were also detected [65,66]. According to the decomposition of the W4f spectra into W^{4+} and W^{6+} states, tungsten is preferentially present in the 4+ state, and its portion in the $Ni_1Mo_{0.5}W_{0.5}$–PC and $Ni_1Mo_{0.5}W_{0.5}$–HT–3 catalysts is as high as 68.9 and 69.9%, respectively. Tungsten is also present in the W^{6+} state. The $Ni_1Mo_{0.5}W_{0.5}$–dry catalyst contains the highest amount of the W^{4+} component (85.9%) and, consequently, the highest amount of W in the active sulfide phase.

Obvious differences between the studied catalysts are observed in the Ni2p spectra. The spectra were decomposed into three components: NiMoWS (Ni2$p_{3/2}$—854.0 ± 0.1 eV), NiS (Ni2$p_{3/2}$—852.8 ± 0.1 eV) and Ni^{2+} (856.0 ± 0.1 eV) [64,67–69]. The prevalence of nickel in the composition of nickel sulfide (55.9%) was detected in the $Ni_1Mo_{0.5}W_{0.5}$–PC sample, while the NiMoWS phase content is about 19%. On the contrary, the $Ni_1Mo_{0.5}W_{0.5}$–HT–3 sample shows another tendency. The NiMoWS content is about 47.9%. Such an increase in the nickel content in the active phase composition may also be related to the possible formation of mixed oxides in the dried sample of the precursor. These data are confirmed by the XRD data. The $Ni_1Mo_{0.5}W_{0.5}$–dry catalyst is similar to the $Ni_1Mo_{0.5}W_{0.5}$–PC catalyst in the Ni state; the prevalence Ni state is Ni sulfide.

The XPS data also show a significant difference in the Mo/S, Ni/S, W/Mo and W/Ni ratios between the $Ni_1Mo_{0.5}W_{0.5}$–HT–3 and $Ni_1Mo_{0.5}W_{0.5}$–PC samples (Table 2). According to the obtained data, Mo is less sulfided in the $Ni_1Mo_{0.5}W_{0.5}$–HT–3 and the $Ni_1Mo_{0.5}W_{0.5}$–dry catalysts. However, these catalysts also contain the highest amount of Mo in the most active 4+ state. The Ni/S ratio is also lower in the $Ni_1Mo_{0.5}W_{0.5}$–HT–3 and the $Ni_1Mo_{0.5}W_{0.5}$–dry catalysts. This may be caused by the fact that Ni in the $Ni_1Mo_{0.5}W_{0.5}$–PC catalyst forms more bulk sulfides that contain more sulfur atoms. It is not clear why the $Ni_1Mo_{0.5}W_{0.5}$–HT–3 and the $Ni_1Mo_{0.5}W_{0.5}$–dry catalysts are characterized by higher W/Mo and W/Ni ratios. It can be supposed that the particles in the $Ni_1Mo_{0.5}W_{0.5}$–PC sample are not porous (as shown in the SEM images), and W may be enclosed in the center. Therefore, the XPS method does not detect W on the particle surface. Such enrichment of W in the center of particles is a possible reason for the poor catalytic activity of the $Ni_1Mo_{0.5}W_{0.5}$–PC sample.

Combining all the results, we can conclude that the lowest activity of the $Ni_1Mo_{0.5}W_{0.5}$–PC catalyst in the studied series is caused by the formation of Ni–Mo particles that are not doped by W, resulting in a decrease in the portion of mixed Ni–Mo–W sulfide phase. Catalysts of hydrothermal series do not considerably differ in activity, but it was noted that the lower crystallinity of the Ni–containing phase is in accordance with the higher activity of catalysts in the HDS and HDN reactions. Moreover, the reagents used for the preparation of the $Ni_1Mo_{0.5}W_{0.5}$–HT–1 catalyst are preferable because fewer individual oxides are formed. The best catalyst in the series is the $Ni_1Mo_{0.5}W_{0.5}$–dry sample. In spite of its high weight loss upon ignition, the catalyst has the highest activity in HDS and HDN reactions. It is possible that the use of chelating agent results in a more uniform distribution of Ni, Mo and W in the catalyst, which are probably dispersed in the carbon matrix (based on XRD data). According to XPS analysis data, this catalyst contains the highest amount of Mo (100%) and W (85.9%) in their most active sulfide states. Therefore, we can conclude that this preparation technique forms a unique composition that provides unprecedently high catalytic activity in the addressed hydrotreatment reactions.

3. Materials and Methods

3.1. Materials for the Preparation of Bulk Catalyst Precursors

The following reagents were used to synthesize the bulk catalyst precursors: nickel (II) nitrate hexahydrate $Ni(NO_3)_3 \times 6H_2O$ (Baltic Enterprise, Ltd., 99%, Saint Petersburg, Russia), basic nickel(II) carbonate $NiCO_3 \times nNi(OH)_2 \times mH_2O$ (Aldrich, 99%), nickel(II) hydroxide $Ni(OH)_2$ (Acron Organics, 99%), ammonium heptamolybdate tetrahydrate (AHM) $(NH_4)_6Mo_7O_{24} \times 4H_2O$ (99%), ammonium metatungstate hydrate (AMT) $(NH_4)_6H_2W_{12}O_{40} \times xH_2O$ (Baltic Enterprise Ltd., 99%), molybdenum(VI) oxide MoO_3 (Baltic Enterprise Ltd., %, Saint Petersburg, Russia), tungstic(VI) acid H_2WO_4 (%) and citric acid (CA) (JSC “Base No. 1 of Chemical Reagents”).

3.2. Preparation of Bulk Catalyst Precursors

Bulk catalyst precursors were prepared using three methods: hydrothermal synthesis, the direct precipitation method and spray drying of the solution with the precursor.

Hydrothermal synthesis of catalyst precursors was performed according to the procedure described in [70]. First, 30 g of basic nickel (II) carbonate, 17.3 g of MoO_3 and 28 g of H_2WO_4 were added to 1 L of deionized water. The resulting suspension was stirred for 15 min and placed in a Parr 4520 autoclave (USA, Parr Instrument Company, Moline, IL, USA) with a total volume of 2 L. The suspension was heated to 170 °C at a rate of 10 °C/min and maintained at that temperature for 6 h under continuous stirring. The hydrothermal treatment temperature was varied between 95, 150 and 170 °C. After the hydrothermal treatment, the autoclave was cooled to room temperature, and the resulting suspension was filtered. The obtained sample was washed with water and dried at 110 °C. A description of the samples, which are designated as $Ni_1Mo_{0.5}W_{0.5}$–HT–x (x = 1–4), is given in Table 1. The ICP analysis data show that precursors contained 21.6–22.5 wt.% Ni, 18.3–19.2 wt.% Mo and 34.3–35.0 wt.% W. It should be noted that temperatures of hydrothermal treatment were chosen for comparison based on the data in the Patent [16]. The patent discloses a method for producing precursors of bulk catalysts by hydrothermal synthesis from commercially available and inexpensive reactants (MoO_3, $2NiCO_3 \times 3Ni(OH)_2$, H_2WO_4, etc.). The hydrothermal synthesis temperatures used in this patent were 90, 150 and 175 °C.

Precursors were synthesized by the method of direct precipitation according to the procedure reported in [71]. To this end, 15.1 g of AHM, 21.7 g of AMT and 50 g of $Ni(NO_3)_3 \cdot 6H_2O$ were dissolved in 200 cm^3 of deionized water. About 500 mL of concentrated NH_4OH solution was added to this solution. Precipitation was initially observed. However, the further addition of NH_4OH led to its dissolution and the formation of a transparent blue solution. Then, the solution was heated to 90 °C and boiled until the pH reached 7. The evaporation of the solution led to the formation of gaseous ammonia and green residue. The resulting suspension was cooled to room temperature and filtered. The powder sample was washed with water and dried at 110 °C for 4 h. This sample was designated as $Ni_1Mo_{0.5}W_{0.5}$–PC (Table 1). The ICP analysis data show that precursors contained 21.1 wt.% Ni, 18.5 wt.% Mo and 35.5 wt.% W.

The third type of synthesis was conducted according to the procedure described in [6]. Citric acid was dissolved in distilled water under intense stirring at 70 °C. Then, nickel hydroxide was added to the solution and stirred until complete dissolution to afford a transparent green solution. AHM and AMT were added to the solution and stirred until complete dissolution. The Ni/CA molar ratio was 1.5 in all solutions. The Ni/Mo/W molar ratio was 1/0.5/0.5. The resulting solutions were spray-dried to obtain the precursor of the active phase of the bulk catalyst. The dried precursor powder was calcined at 390 °C to remove the chelating agent. ICP analysis data show that the precursors contained 21.9 wt.% Ni, 18.8 wt.% Mo and 34.3 wt.% W.

3.3. Testing Bulk Catalyst Precursors in the Hydrotreatment of SRGO

Bulk catalyst precursors were tested in the hydrotreatment of straight-run gasoil (SR GO). To this end, 2 g of catalysts was loaded into a fixed-bed reactor. Catalysts were used in the powder form as they were obtained after drying. A catalyst sample was diluted by SiC (F80) and charged in the isothermal zone of the reactor. SiC (F14) was loaded on the top and bottom of the reactor. The downflow operation mode was used. Such behavior corresponds to a trickle-bed reactor.

The sulfidation of catalysts was carried out under the following conditions: sulfidation mixture: 20 g of DMDS in 1 L of SR GO; pressure: 3.5 MPa; hydrogen/sulfidation mixture ratio: 300 Nl/L; liquid hour space velocity (LHSV) of the sulfidation mixture: 2 h^{-1}; stepwise elevated temperature: 140, 240 and 340 °C. These conditions are typical for the sulfidation of hydrotreating catalysts [72].

After sulfidation, the sulfidation mixture was replaced by SR GO (0.25% S, 160 ppm N, e.b.p. 420 °C). Catalytic tests were carried out under the following conditions: temperature: 330, 340 and 350 °C; pressure: 3.5 MPa; hydrogen/sulfidation mixture ratio: 400 Nl/L; LHSV of SR GO: 2.5 h^{-1}. The catalysts were tested for 24 h at each temperature. There were no liquid samples during first 12 h at each temperature. This period of time was marked as no steady state. Then, six liquid product samples were selected for analysis. The contents of total nitrogen (total N content) and total sulfur (total S content) in the feedstock and hydrotreating products were determined by an Xplorer-NS analyzer (TE Instruments) using oxidative combustion with chemiluminescence and ultraviolet fluorescence detection according to ASTM D5762, ASTM D4629 (for total N content) and ASTM D5453 (for total S content). The total inaccuracy of the analysis was ±1 ppm.

The weight loss of catalysts upon ignition at 550 °C differed significantly (Table 1), the actual weight of loaded metals also differed between the catalysts. Therefore, the *HDS* rate constant (k_{HDS}) was calculated to estimate the *HDS* catalytic activity using Equation (1):

$$k_{HDS} = \frac{-F_s}{W} \ln(1 - X_s) \tag{1}$$

where k_{HDS} is the pseudo-first-order reaction constant for *S*–compound *HDS* (mol g^{-1} h^{-1}); X_S is the conversion (%) of *S*–compounds; F_s is the reactant *S*–compound flow (mol h^{-1}); and *W* is the weight of the catalyst (g), taking into account the weight loss upon ignition.

The conversion of *S*–compounds was calculated using the following Equation (2):

$$X_s = \frac{C_0 - C}{C_0} \times 100 \tag{2}$$

where C_0 is the initial sulfur content in the feedstock, and C is the residual sulfur content in the hydrotreated product.

3.4. Characterization Techniques

Morphology measurements were conducted on a TESCAN SOLARIS FE–SEM Bi–beam scanning electron microscope (TESCAN, Brno, Czech Republic) with 20 kV acceleration in secondary electron mode. The instrument was equipped with an AztecLive energy-dispersive X-ray spectrometer (EDX) with characteristic radiation (Oxford Instruments, Oxford, UK) and a semiconductor Si detector with a resolution of 128 eV.

The X-ray diffraction experiments were carried in transmission mode out using MoKα radiation (λ = 0.7093 Å) on an STOE STADI MP (STOE, Darmstadt, Germany) with a MYTHEN2 1K detector. The measurements were performed in scanning mode in the angle range of 2–69° at 0.015° 2Θ.

The Raman spectra were registered with the use of a LabRAM HR spectrometer (Evolution, Horiba) equipped with a multichannel CCD detector, which was cooled by liquid nitrogen. The spectra were excited by a 633 nm He–Ne laser with a power of about 0.5 mw on the sample surface. The diameter of the laser light spot on the sample surface was about 2 μm. The scattering geometry was 180°. The spectrometer resolution was 2.4 cm^{-1}.

The optical properties of the materials were studied by diffuse reflection electron spectroscopy using a Shimadzu UV-2501 PC spectrophotometer with an ISR-240 A diffuse reflection attachment. The samples (fraction < 0.25 mm) were placed in a quartz cell with a 2 mm optical path length. The spectra were recorded relative to the $BaSO_4$ reflectance standard in the wavelength range of 190–900 nm at room temperature with a 2 nm step. The reflection coefficients were converted using the Kubelka-Munk function, i.e., $F(R) = (1 - R)^2/2R$, where R is the diffuse reflection coefficient dependent on the wavenumber (cm^{-1}). The obtained data are given as coordinates: Kubelka-Munk function F(R)—wavelength.

The photoelectron spectra were registered by a SPECS photoelectron spectrometer (Germany) with a PHOIBOS-150-MCD-9 semispherical energy analyzer and AlKα radiation (hν = 1486.6 eV, 200 W). The binding energy scale was initially calibrated by the peak position of the base levels: $Au4f_{7/2}$ (84.0 eV) and $Cu2p_{3/2}$ (932.7 eV). The peak binding energies were calibrated according to the position of the C1s peak (BE = 284.8 eV). The survey spectra were recorded at the analyzer transmission energy of 50 eV and 20 eV for narrow spectral regions. A low-energy electron gun (FG-15/40, SPECS) was used to neutralize the sample charge.

Thermal analysis of the sample was carried out with an STA 449 C synchronous thermal analysis instrument (Jupiter company NETZSCH). The powder sample was placed into a corundum crucible. The air flow into the chamber was 30 mL/min. The sample was heated in a programmable temperature mode at the rate of 10 °C/min from 30 to 600 °C.

4. Conclusions

In the present study, Ni–Mo–W bulk catalyst precursors were prepared using different methods: hydrothermal synthesis, precipitation method and spray drying after the synthesis of complex compounds in solution. In all cases, bulk catalyst precursors contained particles with a shape similar to spheres or stacked plates. The uniform distribution of molybdenum, tungsten and nickel was observed in all cases (according to the EDX data).

It was established that the synthesis procedure strongly affects the formation of oxide precursor in bulk catalysts and mutual distribution of active metals in Ni–Mo–W particles. The XRD data of the oxide precursors show that the active metals in the samples obtained using hydrothermal synthesis were preferentially included in individual (WO_3 or $W_{17}O_{47}$) or mixed ($W_{1-x}Mo_xO_3$) oxides or in the form of different molybdates ($NiMoO_4$ or $WMoO_4$). The sample prepared by the precipitation method does not have a tungsten-containing phase, while the sample obtained by spray drying after the synthesis of complex compounds in solution contains α–$NiMoO_4$, WO_3, $NiWO_4$ and NiO phases.

The influence of the hydrothermal treatment temperature (95, 150 and 170 °C) and the type of reagents used for synthesis on the properties of Ni–Mo–W bulk catalyst precursors was also studied in this work. According to the XRD results, the hydrothermal treatment temperature mostly influences the formation of $NiW(Mo)O_4$ phases. Their formation was detected at 150 and 170 °C, while no $NiW(Mo)O_4$ phases appeared at 95 °C.

The influence of preparation conditions on the formation of oxide precursor in bulk catalysts was also confirmed by Raman and UV-vis measurements. The spectra of catalysts prepared under hydrothermal conditions at 170 and 150 °C show that active metals are stabilized in $NiMoO_4$ and $NiWO_4$ phases, which correlates with the XRD data. The data of the sample prepared under hydrothermal conditions at 95 °C show a decrease in crystallinity of $NiMoO_4$ and $NiWO_4$ phases and that part of the nickel converts into an X-ray-amorphous NiO phase. The samples prepared by the precipitation method and spray drying after the synthesis of complex compounds in solution also contain $NiMoO_4$ and $NiWO_4$ compounds. However, the ratio of these phases differs depending on the case.

The testing of catalysts in hydrotreatment of straight-run gasoil revealed that the bulk catalyst precursor prepared by spray drying after the synthesis of complex compounds in solution has the highest activity in HDS and HDN reactions. The worst activity was observed for the sample prepared by the precipitation method. The low catalyst activity was mostly attributed to the low content of the mixed Ni–Mo–W sulfide phase and uneven distribution of active metals in catalysts.

Author Contributions: Data curation, K.A.N., S.V.B., Y.V.V., P.P.M., E.Y.G., V.P.P., I.P.P. and T.V.L.; Conceptualization, K.A.N., S.V.B., Y.V.V. and P.P.M.; Writing, K.A.N., S.V.B., Y.V.V., P.P.M. and V.V.A.; validation and formal analysis, K.A.N., S.V.B., Y.V.V., P.P.M., E.Y.G., V.P.P., I.P.P. and T.V.L.; Supervision and project administration, O.V.K., A.S.N. and V.V.A. All authors have read and agreed to the published version of the manuscript.

Funding: This study was funded by the Russian Science Foundation as part of research project № 22-73-10144 (https://rscf.ru/en/project/22-73-10144/).

Data Availability Statement: All data included in this study are available upon request by contact with the first author or corresponding author.

Conflicts of Interest: The authors declare no conflict of interest.

Abbreviations

HDS—hydrodesulfurization; HDN—hydrodenitrogenation; SEM—scanning electron microscopy; EDX—energy–dispersive X-ray; XRD—X-ray diffraction; DXRD—coherent scattering region; UV-vis DRS—ultraviolet–visible diffuse reflectance spectroscopy; LMCT—ligand-to-metal charge transfer; TG—thermogravimetry; DTG—derivative thermogravimetry; XPS—X-ray photoelectron spectroscopy; AHM—ammonium heptamolybdate tetrahydrate; AMT—ammonium metatungstate hydrate; CA—citric acid; SR GO—straight-run gasoil; LHSV—liquid hour space velocity; DMDS—dimethyl disulfide.

References

1. Gochi, Y.; Alvarez-Contreras, L.; Paraguay-Delgado, F.; Alonso-Nunez, G. Influence of the Presence of Al_2O_3 on Ni–Mo–W Trimetallic Catalysts for HDS. *Int. J. Mater. Prod. Technol.* **2006**, *27*, 130–140. [CrossRef]
2. Plantenga, F.L.; Cerfontain, R.; Eijsbouts, S.; Houtert, F.; Anderson, G.H.; Miseo, S.; Soled, S.; Riley, K.; Fujita, K.; Inoue, Y. "NEBULA": A Hydroprocessing Catalyst with Breakthrough Activity. *Stud. Surf. Sci. Catal.* **2003**, *145*, 407–410. [CrossRef]
3. Eijsbouts, S.; Mayo, S.; Fujita, K. Unsupported Transition Metal Sulfide Catalysts: From Fundamentals to Industrial Application. *Appl. Catal. A General* **2007**, *322*, 58–66. [CrossRef]
4. Yu, H.; Zhang, J.; Nan, J.; Geng, S.; Zhang, Y.; Shi, Y.; Qu, X.; Liu, H. Synthesis and Hydrodesulfurization Performance of Bulk Ni–Mo–W Catalyst with High Surface Area. *Adv. Mater. Res.* **2013**, *634–638*, 604–607. [CrossRef]
5. Yin, C.; Wang, Y.; Xue, S.; Liu, H.; Li, H.; Liu, C. Influence of Sulfidation Conditions on Morphology and Hydrotreating Performance of Unsupported Ni–Mo–W Catalysts. *Fuel* **2016**, *175*, 13–19. [CrossRef]
6. Nadeina, K.A.; Budukva, S.V.; Vatutina, Y.V.; Mukhacheva, P.P.; Gerasimov, E.Y.; Pakharukova, V.P.; Klimov, O.V.; Noskov, A.S. Unsupported Ni–Mo–W Hydrotreating Catalyst: Influence of the Atomic Ratio of Active Metals on the HDS and HDN Activity. *Catalysts* **2022**, *12*, 1671. [CrossRef]
7. Licea, Y.E.; Grau-Crespo, R.; Palacio, L.A.; Faro, A.C. Unsupported Trimetallic Ni(Co)–Mo–W Sulphide Catalysts Prepared from Mixed Oxides: Characterisation and Catalytic Tests for Simultaneous Tetralin HDA and Dibenzothiophene HDS Reactions. *Catal. Today* **2017**, *292*, 84–96. [CrossRef]
8. Arias, S.; Licea Fonseca, Y.; Soares, D.; Eon, J.-G.; Palacio, L.; Faro, A., Jr. Mixed NiMo, NiW and NiMoW Sulfides Obtained from Layered Double Hydroxides as Catalysts in Simultaneous HDA and HDS Reactions. *Catal. Today* **2017**, *296*, 187–196. [CrossRef]
9. Wang, C.; Wu, Z.; Tang, C.; Li, L.; Wang, D. The Effect of Nickel Content on the Hydrodeoxygenation of 4–Methylphenol over Unsupported NiMoW Sulfide Catalysts. *Catal. Commun.* **2013**, *32*, 76–80. [CrossRef]
10. Yi, Y.; Zhang, B.; Jin, X.; Wang, L.; Williams, C.T.; Xiong, G.; Su, D.S.; Liang, C. Unsupported NiMoW Sulfide Catalysts for Hydrodesulfurization of Dibenzothiophene by Thermal Decomposition of Thiosalts. *J. Mol. Catal. A Chemical* **2011**, *351*, 120–127. [CrossRef]
11. Sizova, I.; Kulikov, A.; Onishchenko, M.; Serdyukov, S.; Maksimov, A. Synthesis of Nickel–Tungsten Sulfide Hydrodearomatization Catalysts by the Decomposition of Oil–Soluble Precursors. *Pet. Chem.* **2016**, *56*, 44–50. [CrossRef]
12. Topsøe, H.; Clausen, B.S.; Candia, R.; Wivel, C.; Mørup, S. In Situ Mössbauer Emission Spectroscopy Studies of Unsupported and Supported Sulfided Co–Mo Hydrodesulfurization Catalysts: Evidence for and Nature of a Co–Mo–S Phase. *J. Catal.* **1981**, *68*, 433–452. [CrossRef]
13. Huirache-Acuña, R.; Albiter, M.A.; Espino, J.; Ornelas, C.; Alonso-Nuñez, G.; Paraguay-Delgado, F.; Rico, J.L.; Martínez-Sánchez, R. Synthesis of Ni–Mo–W Sulphide Catalysts by Ex Situ Decomposition of Trimetallic Precursors. *Appl. Catal. A Gen.* **2006**, *304*, 124–130. [CrossRef]
14. Pinaeva, L.; Prosvirin, I.; Chesalov, Y.; Atuchin, V. High–Temperature Abatement of N2O over FeOx/CeO_2–Al_2O_3 Catalysts: The Effects of Oxygen Mobility. *Catalysts* **2022**, *12*, 938. [CrossRef]
15. Albersberger, S.; Hein, J.; Schreiber, M.W.; Guerra, S.; Han, J.; Gutiérrez, O.Y.; Lercher, J.A. Simultaneous Hydrodenitrogenation and Hydrodesulfurization on Unsupported Ni–Mo–W Sulfides. *Catal. Today* **2017**, *297*, 344–355. [CrossRef]
16. Soled, S.L.; Miseo, S.; Eijsbouts, S.; Plantenga, F.L. Bulk Bimetallic Catalysts, Method of Making Bulk Bimetallic Catalysts and Hydroprocessing Using Bulk Bimetallic Catalysts. U.S. Patent 7648941, 19 January 2010.
17. Yin, C.; Wang, Y. Effect of Sulfidation Process on Catalytic Performance over Unsupported Ni–Mo–W Hydrotreating Catalysts. *Korean J. Chem. Eng.* **2017**, *34*, 1004–1012. [CrossRef]
18. Amaya, S.L.; Alonso-Núñez, G.; Zepeda, T.A.; Fuentes, S.; Echavarría, A. Effect of the Divalent Metal and the Activation Temperature of NiMoW and CoMoW on the Dibenzothiophene Hydrodesulfurization Reaction. *Appl. Catal. B Environ.* **2014**, *148–149*, 221–230. [CrossRef]
19. Yue, L.; Li, G.; Zhang, F.; Chen, L.; Li, X.; Huang, X. Size–Dependent Activity of Unsupported Co–Mo Sulfide Catalysts for the Hydrodesulfurization of Dibenzothiophene. *Appl. Catal. A Gen.* **2016**, *512*, 85–92. [CrossRef]
20. Chen, Y.; Wang, L.; Zhang, Y.; Liu, T.; Liu, X.; Jiang, Z.; Li, C. A New Multi–Metallic Bulk Catalyst with High Hydrodesulfurization Activity of 4,6–DMDBT Prepared Using Layered Hydroxide Salts as Structural Templates. *Appl. Catal. A Gen.* **2014**, *474*, 69–77. [CrossRef]
21. Liu, H.; Liu, C.; Yin, C.; Chai, Y.; Li, Y.; Liu, D.; Liu, B.; Li, X.; Wang, Y.; Li, X. Preparation of Highly Active Unsupported Nickel–Zinc–Molybdenum Catalysts for the Hydrodesulfurization of Dibenzothiophene. *Appl. Catal. B Environ.* **2015**, *174–175*, 264–276. [CrossRef]
22. Yin, C.; Zhao, L.; Bai, Z.; Liu, H.; Liu, Y.; Liu, C. A Novel Porous Ammonium Nickel Molybdate as the Catalyst Precursor towards Deep Hydrodesulfurization of Gas Oil. *Fuel* **2013**, *107*, 873–878. [CrossRef]
23. Vatutina, Y.V.; Kazakov, M.O.; Nadeina, K.A.; Budukva, S.V.; Danilova, I.G.; Gerasimov, E.Y.; Suprun, E.A.; Prosvirin, I.P.; Nikolaeva, O.A.; Gabrienko, A.A.; et al. Is It Possible to Reactivate Hydrotreating Catalyst Poisoned by Silicon? *Catal. Today* **2021**, *378*, 43–56. [CrossRef]
24. Eijsbouts, S.; van den Oetelaar, L.C.A.; Rayner, M.; Govaers, H.; Boonen, T. Combined HR TEM and STEM–EDX Evaluation—The Key to Better Understanding of the Co–Mo Sulfide Active Phase in Real–Life Co–Mo–P/Al_2O_3 Catalysts. *J. Catal.* **2021**, *403*, 56–73. [CrossRef]

25. Oudghiri Hassani, H.; Wadaani, F. Preparation, Characterization and Catalytic Activity of Nickel Molybdate ($NiMoO_4$) Nanoparticles. *Molecules* **2018**, *23*, 273. [CrossRef]
26. Sharma, P.; Minakshi, M.; Whale, J.; Jean-Fulcrand, A.; Garnweitner, G. Effect of the Anionic Counterpart: Molybdate vs. Tungstate in Energy Storage for Pseudo–Capacitor Applications. *Nanomaterials* **2021**, *11*, 580. [CrossRef]
27. Wang, X.-X.; Li, Y.; Liu, M.-C.; Kong, L.-B. Fabrication and Electrochemical Investigation of MWO_4 (M = Co, Ni) Nanoparticles as High–Performance Anode Materials for Lithium–Ion Batteries. *Ionics* **2018**, *24*, 363–372. [CrossRef]
28. Niu, L.; Li, Z.; Xu, Y.; Sun, J.; Hong, W.; Liu, X.; Wang, J.; Yang, S. Simple Synthesis of Amorphous $NiWO_4$ Nanostructure and Its Application as a Novel Cathode Material for Asymmetric Supercapacitors. *ACS Appl. Mater. Interfaces* **2013**, *5*, 8044–8052. [CrossRef]
29. Dabbous, S.; Ben Nasrallah, T.; Ouerfelli, J.; Boubaker, K.; Amlouk, M.; Belgacem, S. Study of Structural and Optical Properties of Sprayed WO_3 Thin Films Using Enhanced Characterization Techniques along with the Boubaker Polynomials Expansion Scheme (BPES). *J. Alloys Compd.* **2009**, *487*, 286–292. [CrossRef]
30. Famili, Z.; Dorranian, D.; Sari, A.H. Laser Ablation–Assisted Synthesis of Tungsten Sub–Oxide ($W_{17}O_{47}$) Nanoparticles in Water: Effect of Laser Fluence. *Opt. Quant. Electron.* **2020**, *52*, 305. [CrossRef]
31. Levin, D.; Soled, S.L.; Ying, J.Y. Crystal Structure of an Ammonium Nickel Molybdate Prepared by Chemical Precipitation. *Inorg. Chem.* **1996**, *35*, 4191–4197. [CrossRef]
32. Amaya, S.L.; Alonso-Núñez, G.; Cruz-Reyes, J.; Fuentes, S.; Echavarría, A. Influence of the Sulfidation Temperature in a NiMoW Catalyst Derived from Layered Structure $(NH_4)Ni_2OH(H_2O)(MoO_4)_2$. *Fuel* **2015**, *139*, 575–583. [CrossRef]
33. García-Pérez, D.; Blanco-Brieva, G.; Alvarez-Galvan, M.C.; Campos-Martin, J.M. Influence of W Loading, Support Type, and Preparation Method on the Performance of Zirconia or Alumina–Supported Pt Catalysts for n–Dodecane Hydroisomerization. *Fuel* **2022**, *319*, 123704. [CrossRef]
34. Rico, J.L.; Albiter, M.; Espino, J.; Hargreaves, J.S.J.; Ostroumov, M.; Salcedo, L.I.; Wilson, K. Synthesis and Ammonolysis of Nickel and Cobalt Tungstates and Their Characterisation. *J. Saudi Chem. Soc.* **2016**, *20*, 405–410. [CrossRef]
35. Marins, A.A.L.; Banhos, S.G.; Muri, E.J.B.; Rodrigues, R.V.; Cruz, P.C.M.; Freitas, M.B.J.G. Synthesis by Coprecipitation with Oxalic Acid of Rare Earth and Nickel Oxides from the Anode of Spent Ni–MH Batteries and Its Electrochemical Properties. *Mater. Chem. Phys.* **2020**, *242*, 122440. [CrossRef]
36. Popovych, O.M.; Budzulyak, I.M.; Yukhymchuk, V.O.; Budzulyak, S.I.; Popovych, D.I. Raman Spectroscopy of Nickel Molybdate and Its Modifications. *Fuller. Nanotub. Carbon Nanostructures* **2021**, *29*, 1009–1015. [CrossRef]
37. Atuchin, V.V.; Aleksandrovsky, A.S.; Chimitova, O.D.; Gavrilova, T.A.; Krylov, A.S.; Molokeev, M.S.; Oreshonkov, A.S.; Bazarov, B.G.; Bazarova, J.G. Synthesis and Spectroscopic Properties of Monoclinic A–$Eu_2(MoO_4)$. *J. Phys. Chem. C* **2014**, *118*, 15404–15411. [CrossRef]
38. Zhao, P.; Murshed, M.M.; Alekseev, E.V.; Atuchin, V.V.; Pugachev, A.M.; Gesing, T.M. Synthesis, Structure and Properties of $Na[AsW_2O_9]$. *Mater. Res. Bull.* **2014**, *60*, 258–263. [CrossRef]
39. Alekseev, E.V.; Felbinger, O.; Wu, S.; Malcherek, T.; Depmeier, W.; Modolo, G.; Gesing, T.M.; Krivovichev, S.V.; Suleimanov, E.V.; Gavrilova, T.A.; et al. $K[AsW_2O_9]$, the First Member of the Arsenate–Tungsten Bronze Family: Synthesis, Structure, Spectroscopic and Non–Linear Optical Properties. *J. Solid State Chem.* **2013**, *204*, 59–63. [CrossRef]
40. Prosnikov, M.A.; Davydov, V.Y.; Smirnov, A.N.; Volkov, M.P.; Pisarev, R.V.; Becker, P.; Bohatý, L. Lattice and Spin Dynamics in a Low–Symmetry Antiferromagnet $NiWO_4$. *Phys. Rev. B* **2017**, *96*, 014428. [CrossRef]
41. Zhang, C.C.; Zheng, L.; Zhang, Z.M.; Dai, R.C.; Wang, Z.P.; Zhang, J.W.; Ding, Z.J. Raman Studies of Hexagonal MoO_3 at High Pressure. *Phys. Status Solidi.* **2011**, *248*, 1119–1122. [CrossRef]
42. Atuchin, V.V.; Gavrilova, T.A.; Grigorieva, T.I.; Kuratieva, N.V.; Okotrub, K.A.; Pervukhina, N.V.; Surovtsev, N.V. Sublimation Growth and Vibrational Microspectrometry of α–MoO_3 Single Crystals. *J. Cryst. Growth* **2011**, *318*, 987–990. [CrossRef]
43. Díaz-Reyes, J.; Castillo-Ojeda, R.; Galván-Arellano, M.; Zaca-Moran, O. Characterization of WO_3 Thin Films Grown on Silicon by HFMOD. *Adv. Condens. Matter Phys.* **2013**, *2013*, 591787. [CrossRef]
44. Budukva, S.V.; Klimov, O.V.; Uvarkina, D.D.; Chesalov, Y.A.; Prosvirin, I.P.; Larina, T.V.; Noskov, A.S. Effect of Citric Acid and Triethylene Glycol Addition on the Reactivation of CoMo/γ–Al_2O_3 Hydrotreating Catalysts. *Catal. Today* **2019**, *329*, 35–43. [CrossRef]
45. Duan, A.; Li, R.; Jiang, G.; Gao, J.; Zhao, Z.; Wan, G.; Zhang, D.; Huang, W.; Chung, K.H. Hydrodesulphurization Performance of NiW/TiO_2–Al_2O_3 Catalyst for Ultra Clean Diesel. *Catal. Today* **2009**, *140*, 187–191. [CrossRef]
46. Gutiérrez-Alejandre, A.; Ramírez, J.; Busca, G. The Electronic Structure of Oxide–Supported Tungsten Oxide Catalysts as Studied by UV Spectroscopy. *Catal. Lett.* **1998**, *56*, 29–33. [CrossRef]
47. Liu, Z.; Chen, Y. Spectroscopic Studies on Tetragonal ZrO_2–Supported MoO_3 and NiO−MoO_3 Systems. *J. Catal.* **1998**, *177*, 314–324. [CrossRef]
48. Suárez-Toriello, V.A.; Santolalla-Vargas, C.E.; De Los Reyes, J.A.; Vázquez-Zavala, A.; Vrinat, M.; Geantet, C. Influence of the Solution PH in Impregnation with Citric Acid and Activity of Ni/W/Al_2O_3 Catalysts. *J. Mol. Catal. A Chem.* **2015**, *404–405*, 36–46. [CrossRef]
49. Ross-Medgaarden, E.I.; Wachs, I.E. Structural Determination of Bulk and Surface Tungsten Oxides with UV−vis Diffuse Reflectance Spectroscopy and Raman Spectroscopy. *J. Phys. Chem. C* **2007**, *111*, 15089–15099. [CrossRef]

50. Tian, H.; Roberts, C.A.; Wachs, I.E. Molecular Structural Determination of Molybdena in Different Environments: Aqueous Solutions, Bulk Mixed Oxides, and Supported MoO_3 Catalysts. *J. Phys. Chem. C* **2010**, *114*, 14110–14120. [CrossRef]
51. Gajbhiye, N.S.; Balaji, G. Synthesis, Reactivity, and Cations Inversion Studies of Nanocrystalline $MnFe_2O_4$ Particles. *Thermochim. Acta* **2002**, *385*, 143–151. [CrossRef]
52. Bocher, L.; Aguirre, M.H.; Robert, R.; Trottmann, M.; Logvinovich, D.; Hug, P.; Weidenkaff, A. Chimie Douce Synthesis and Thermochemical Characterization of Mesoporous Perovskite–Type Titanate Phases. *Thermochim. Acta* **2007**, *457*, 11–19. [CrossRef]
53. Rajendran, M.; Rao, M.S. Formation of $BaTiO_3$ from Citrate Precursor. *J. Solid State Chem.* **1994**, *113*, 239–247. [CrossRef]
54. Rajendran, M.; Rao, S.M. Synthesis and Characterization of Barium Bis(Citrato) Oxozirconate(IV) Tetrahydrate: A New Molecular Precursor for Fine Particle $BaZrO_3$. *J. Mater. Res.* **1994**, *9*, 2277–2284. [CrossRef]
55. Kovács, T.N.; Hunyadi, D.; de Lucena, A.L.A.; Szilágyi, I.M. Thermal Decomposition of Ammonium Molybdates. *J. Therm. Anal. Calorim.* **2016**, *124*, 1013–1021. [CrossRef]
56. Fait, M.J.G.; Lunk, H.-J.; Feist, M.; Schneider, M.; Dann, J.N.; Frisk, T. Thermal Decomposition of Ammonium Paratungstate Tetrahydrate under Non–Reducing Conditions: Characterization by Thermal Analysis, X-ray Diffraction and Spectroscopic Methods. *Thermochim. Acta* **2008**, *469*, 12–22. [CrossRef]
57. Hunyadi, D.; Sajó, I.; Szilágyi, I.M. Structure and Thermal Decomposition of Ammonium Metatungstate. *J. Therm. Anal. Calorim.* **2014**, *116*, 329–337. [CrossRef]
58. Atuchin, V.V.; Aleksandrovsky, A.S.; Chimitova, O.D.; Diao, C.-P.; Gavrilova, T.A.; Kesler, V.G.; Molokeev, M.S.; Krylov, A.S.; Bazarov, B.G.; Bazarova, J.G.; et al. Electronic Structure of β–$RbSm(MoO_4)_2$ and Chemical Bonding in Molybdates. *Dalt. Trans.* **2015**, *44*, 1805–1815. [CrossRef] [PubMed]
59. Qiu, L.; Xu, G. Peak Overlaps and Corresponding Solutions in the X-Ray Photoelectron Spectroscopic Study of Hydrodesulfurization Catalysts. *Appl. Surf. Sci.* **2010**, *256*, 3413–3417. [CrossRef]
60. Romanova, T.S.; Nadeina, K.A.; Danilova, I.G.; Danilevich, V.V.; Pakharukova, V.P.; Gabrienko, A.A.; Glazneva, T.S.; Gerasimov, E.Y.; Prosvirin, I.P.; Vatutina, Y.V.; et al. Modification of HDT Catalysts of FCC Feedstock by Adding Silica to the Kneading Paste of Alumina Support: Advantages and Disadvantages. *Fuel* **2022**, *324*, 124555. [CrossRef]
61. Scott, C.E.; Perez-Zurita, M.J.; Carbognani, L.A.; Molero, H.; Vitale, G.; Guzmán, H.J.; Pereira-Almao, P. Preparation of NiMoS Nanoparticles for Hydrotreating. *Catal. Today* **2015**, *250*, 21–27. [CrossRef]
62. Atuchin, V.; Galashov, E.; Khyzhun, O.; Kozhukhov, A.; Pokrovsky, L.; Shlegel, V. Structural and Electronic Properties of $ZnWO_4$(010) Cleaved Surface. *Cryst. Growth Des.* **2011**, *11*, 2479–2484. [CrossRef]
63. Korobeishchikov, N.G.; Nikolaev, I.V.; Atuchin, V.V.; Prosvirin, I.P.; Kapishnikov, A.V.; Tolstogouzov, A.; Fu, D.J. Quantifying the Surface Modification Induced by the Argon Cluster Ion Bombardment of $KGd(WO_4)_2$: Nd Single Crystal. *Mater. Res. Bull.* **2023**, *158*, 112082. [CrossRef]
64. Ben Tayeb, K.; Lamonier, C.; Lancelot, C.; Fournier, M.; Payen, E.; Bonduelle, A.; Bertoncini, F. Study of the Active Phase of NiW Hydrocracking Sulfided Catalysts Obtained from an Innovative Heteropolyanion Based Preparation. *Catal. Today* **2010**, *150*, 207–212. [CrossRef]
65. Orsini, G.; Tricoli, V. Facile Nonhydrolytic Sol–Gel Route to Mesoporous Mixed–Conducting Tungsten Oxide. *J. Mater. Chem.* **2011**, *21*, 14530–14542. [CrossRef]
66. Ghosh, K.; Roy, A.; Tripathi, S.; Ghule, S.; Singh, A.; Narayanan, R. Insights into Nucleation, Growth and Phase Selection of WO3: Morphology Control and Electrochromic Property. *J. Mater. Chem. C* **2017**, *5*, 7307–7316. [CrossRef]
67. Wang, C.; Zan, X.; Wu, Z.; Wang, Z.; Chaoyun, T.; Zhou, P. Effect of W Addition on the Hydrodeoxygenation of 4–Methylphenol over Unsupported NiMo Sulfide Catalysts. *Appl. Catal. A Gen.* **2014**, *476*, 61–67. [CrossRef]
68. Rodriguez-Castellon, E.; Jiménez-López, A.; Eliche-Quesada, D. Nickel and Cobalt Promoted Tungsten and Molybdenum Sulfide Mesoporous Catalysts for Hydrodesulfurization. *Fuel* **2008**, *87*, 1195–1206. [CrossRef]
69. Hu, F.; Ye, R.; Jin, C.; Liu, D.; Chen, X.; Li, C.; Lim, K.H.; Song, G.; Wang, T.; Feng, G.; et al. Ni Nanoparticles Enclosed in Highly Mesoporous Nanofibers with Oxygen Vacancies for Efficient CO_2 Methanation. *Appl. Catal. B Environ.* **2022**, *317*, 121715. [CrossRef]
70. Soled, S.; Miseo, S.; Eijsbouts, S.; Plantenga, F. Bulk Bimetallic Catalysts, Method of Making Bulk Bimetallic Catalysts and Hydroprocessing Using Bulk Bimetallic Catalysts. U.S. Patent 20070084754, 19 January 2010.
71. Soled, S.L.; Riley, K.L.; Schleicher, G.P. Hydroprocessing Using Bulk Group VIII/Group VIB Catalysts (HEN–9901). U.S. Patent 6162350, 19 December 2020.
72. Nadeina, K.A.; Danilevich, V.V.; Kazakov, M.O.; Romanova, T.S.; Gabrienko, A.A.; Danilova, I.G.; Pakharukova, V.A.; Nikolaeva, O.A.; Gerasimov, E.Y.; Prosvirin, I.P.; et al. Silicon Doping Effect on the Properties of the Hydrotreating Catalysts of FCC Feedstock Pretreatment. *Appl. Catal. B Environ.* **2021**, *280*, 119415. [CrossRef]